CHANNEL MODELLING AND CHARACTERIZATION FOR VLC-BASED MEDICAL BODY SENSOR NETWORKS

BARIŞ DÖNMEZ

IŞIK UNIVERSITY

2022

CHANNEL MODELLING AND CHARACTERIZATION FOR VLC-BASED MEDICAL BODY SENSOR NETWORKS

BARIŞ DÖNMEZ

Electrical and Electronics Engineering, IŞIK UNIVERSITY

Submitted to the Graduate School of Science and Engineering
in partial fulfillment of the requirements for the degree of
Master of Science
in
Electrical and Electronics Engineering

IŞIK UNIVERSITY
2022

IŞIK UNIVERSITY
GRADUATE SCHOOL OF SCIENCE AND ENGINEERING

CHANNEL MODELLING AND CHARACTERIZATION FOR VLC-BASED
MEDICAL BODY SENSOR NETWORKS

BARIŞ DÖNMEZ

APPROVED BY:

Asst. Prof.
Farshad Miramirkhani   Işık University
(Thesis Supervisor)

Prof. Onur Kaya   Işık University

Asst. Prof.
Tunçer Baykaş   Kadir Has University

APPROVAL DATE: 10/01/2022

CHANNEL MODELLING AND CHARACTERIZATION FOR VLC-BASED MEDICAL BODY SENSOR NETWORKS

Abstract

Optical Wireless Communication (OWC) refers to transmission in unguided propagation media through the use of optical carriers, i.e., visible, Infrared (IR), and Ultraviolet (UV) bands. In this thesis, we focus on indoor Visible Light Communication (VLC)-based Medical Body Sensor Networks (MBSNs) which allow the Light Emitting Diodes (LEDs) to communicate between on-body sensors/subdermal implants and on-body central hubs/monitoring devices while also serving as a luminaire. Since the Quality-of-Service (QoS) of the communication systems depends heavily on realistic channel modeling and characterization, this thesis aims at presenting an up-to-date survey of works on channel modeling activities for MBSNs. After the introduction chapter, the second chapter presents the literature survey and the first section reviews existing IR-based MBSNs channel models based on which VLC channel models are derived. The final section of this chapter provides comprehensive details on existing VLC-based MBSNs channel models. Third chapter presents a realistic channel modeling approach called site-specific ray tracing that considers the skin tissue for the MBSNs channel modeling for realistic hospital scenarios. In addition, channel characteristics which are the channel DC gain and RMS delay spread values that are extracted from the sample Channel Impulse Responses (CIRs) among extensive amount of static channel modelling simulations are demonstrated. Fourth chapter proposes a random trajectory generator and implements it in mobile channel modelling and characterization for the two of the aforementioned real-life based scenarios. Then, the CIRs and channel characteristics are obtained then by utilizing the simulation results data, the spatial distribution of channel characteristics and curve fitting on histograms of these are illustrated with explanations.

GÖRÜNÜR IŞIK İLETİŞİMİ TABANLI MEDİKAL VÜCUT SENSÖR AĞLARI İÇİN KANAL MODELLENMESİ VE KARAKTERİZASYONU

Özet

Optik Kablosuz İletişim (OWC), optik taşıyıcılar vasıtasıyla Görünür Işık İletişimi (VLC), Kızılötesi(IR), Morötesi(UV) bantlarında gerçekleşen iletimi ifade etmektedir. Bu tezde, ortam aydınlatan Işık Yayan Diyotlar (LEDs) vasıtasıyla vücut üzerindeki/deri altındaki sensörler ile vücuttaki ana sensör/tıbbi ölçüm cihazları arasındaki iletişimin sağlandığı kapalı alan görünür ışık iletişimi (VLC) tabanlı medikal vücut sensör ağlarına (MBSNs) odaklanmaktayız. İletişim sistemlerinin Servis Kalitesi (QoS) ağırlıklı olarak gerçekçi kanal modellemeleri ve karakterizasyonuna bağlı olduğundan dolayı bu tez en güncel literatür taramasını barındırmaktadır. Giriş bölümünün ardından başlayan literatür taraması bölümünde, ilk olarak VLC tabanlı MBSNs sistemlerinin kanal modellerinin türediği IR tabanlı MBSNs sistemlerinin kanal modelleriyle ilgili çalışmalar ve ikinci kısımda ise ana konumuz olan VLC tabanlı MBSNs sistemleriyle ilgili mevcut çalışmalar oldukça kapsamlı olarak tartışılmıştır. Üçüncü bölümde ise, gerçeğe uygun hastahane senaryolarındaki VLC tabanlı MBSNs sistemlerinin gerçekçi kanal modellemelerinin yapılabilmesi için insan derisi de, mekana özgü ışın izleme metodunu kullanılarak kanal kabul edilerek modellenmiş ve kanal dürtü tepkileri (CIRs) sunulmuştur. Buna ilave olarak, bahsi geçen hastahane senaryolarından simülasyonlar sonucu elde edilen CIRs, Doğru Akım (DC) kanal kazancı ve Karekök Ortalama (RMS) gecikme yayılımı kanal karakterleri de sayıca çok olmasından dolayı tarafımızca seçilen örnekleriyle sunulup tartışılmıştır. Dördüncü bölümde ise, rastlantısal yörünge üreteci önerilmiş ve hastahane senaryolarından en uygun ikisi seçilerek hareketli kanal modellemesi ve karakterizyonu yapılmıştır. Bu simülasyon sonuçları kullanılarak bahsi geçen kanal karakteristiklerinin uzaysal dağılımları, çubuk grafikler üzerindeki eğri uydurmaları sunulmuş ve tartışılmıştır.

Anahtar kelimeler: Kanal modelleme, Medikal Vücut Sensör Ağları, Optik İletişim, Deri İçinden Geçen İletişim, Görülür Işık İletişimi, Hareketli Kanal Modellemesi, Rastlantısal Yörünge

Acknowledgements

I would like to thank my supervisor, Asst. Prof. Farshad Miramirkhani, for his guidance and encouragement during my Master's research. I am thankful to him for helping me to become a true researcher. My sincere gratitude is also reserved for Prof. Onur Kaya who has been much more than a professor to me.

I am truly grateful to the members of my thesis committee, Asst. Prof. Tunçer Baykaş, Prof. Ahmet Aksen, and Assoc. Prof. Ali Emre Pusane for their time serving on my committee and carefully reviewing my dissertation.

I would like to thank my parents, for their unconditional and endless support, inspiration, and encouragement with my studies. I am honored to have them as my parents.

To my family ...

Table of Contents

List of Tables

List of Figures

List of Abbreviations

2D	**2** **D**imensions
3D	**3** **D**imensions
AMI	**A**lternate **M**ark **I**nversion
BRDF	**B**idirectional **R**eflectance **D**istribution **F**unction
CIR	**C**hannel **I**mpulse **R**esponse
ECG	**E**lectro**c**ardio**g**raph
FCPR	**F**amily **C**entered **P**atient **R**oom
FOV	**F**ield **O**f **V**iew
GEV	**G**eneralized **E**xtreme **V**alue
IPS	**I**ndoor **P**ositioning **S**ystems
ITL	**I**nformation **T**heoretic **L**earning
IR	**I**nfra**r**ed
ICU	**I**ntensive **C**are **U**nit
ISI	**I**nter **S**ymbol **I**nterference
LED	**L**ight-**e**mitting **D**iodes
LoS	**L**ine-**o**f-**S**ight
MBSN	**M**edical **B**ody **S**ensor **N**etworks
MCRT	**M**onte **C**arlo **R**ay **T**racing
MISO	**M**ultiple-**I**nput **S**ingle-**O**utput
NLoS	**N**on-**L**ine-**o**f-**S**ight
NZR	**N**on-**R**eturn-to-**Z**ero
OOK	**O**n-**O**ff **K**eying
OTHG	**O**ne-**T**erm **H**enyey-**G**reenstein
OCC	**O**ptical **C**amera **C**ommunication

OCDMA	**O**ptical **C**ode-**D**ivision Multiple-**A**ccess
OOC	**O**ptical **O**rthogonal **C**ode
OWC	**O**ptical **W**ireless **C**ommunications
PD	**P**hoto**d**etector
PPG	**P**hoto**p**lethysmo**g**raph
PDF	**P**robability **D**ensity **F**unction
QoS	**Q**uality-**of**-**S**ervice
RF	**R**adio **F**requency
RW	**R**andom **W**alk
RWP	**R**andom **W**ay**p**oint
RKHS	**R**eproducing **K**ernel **H**ilbert **S**pace
RMS	**R**oot **M**ean **S**quare
SIMO	**S**ingle-**I**nput Multiple-**O**utput
SwC	**Sw**itching **C**ombining
TCCR	**T**hin Film **C**orner **C**ube **R**etroreflector
TOA	**T**ime **O**f **A**rrival
TC	**T**ransdermal **C**ommunications
UV	**U**ltra**v**iolet
VL	**V**isible **L**ight
VLC	**V**isible **L**ight **C**ommunication
ZCC	**Z**ero **C**ross **C**orrelation

Chapter 1

Introduction

Optical Wireless Communication (OWC) has emerged as a promising technology for 6G and beyond communication networks. The optical transmission allows for spatial re-utilization and protection from Radio Frequency (RF) co-channel and inter-symbol interference, and thus is an attractive solution for addressing the existing spectrum crunch in wireless communication. The primary benefits of OWC include ultra-high bandwidth over an unregulated license-free spectrum, ultra-high data rate, and ultra-low latency [1–4]. Among several OWC methods, Visible Light Communication (VLC) refers to signaling within a sub-spectrum of optical spectrum (79 to 430 THz) that is potentially useful for wireless transmission using fast-switching Light-Emitting Diodes (LEDs) in accordance with the input messages. Therefore, for the VLC systems, the LEDs are known to function dually as both optical-transmitters and luminaries.

VLC transcends the traditional RF based systems due to the properties of its physical layer. Firstly, VLC provides a secure communication since the light rays cannot pass through opaque materials. This makes VLC an ideal supplement for RF based systems for indoor applications, such as, Medical Body Sensor Networks (MBSNs) [1–7]. In this regard, the IEC 60601-1-2 standard for VLC MBSN are found to allow for a minimal distance between a medical equipment and RF transceiver to prevent deterioration in the Quality-of-Service (QoS) [8]. In addition, VLC is known to have a large bandwidth. Furthermore, VLC is

unlicensed, which makes its case as an auxiliary technology that potentially eases the typically heavy data traffic in an indoor environment [9].

With intensification of research-activities in VLC, recent surveys review various aspects of VLC. In [3], a comprehensive survey on VLC was provided with an emphasis on challenges such as bandwidth enhancement, interference and noise removal, non-linearity compensation and signal clipping, and optical beamforming faced in indoor applications over the period of 1979-2014. In [10], another survey covered physical layer issues, medium access techniques, system design and programmable platforms, and Visible Light (VL) sensing for indoor applications. In [11], VLC-based Indoor Positioning Systems (IPS) are classified according to an accuracy-analysis of VLC-based-IPS in experimental and simulation environments. In [12], a survey of channel modeling for indoor VLC was published covering five different types of typical indoor VLC channel models with their pros and cons together with their application scenarios. In [13], a survey of OWC channel measurement campaigns and channel models covering indoor, outdoor, underground, and underwater environments was presented. In the existing VLC literature, there are several other papers which address the challenges that could potentially enhance VLC system design and align it with consumer-challenges [14–16].

In the current decade, OWC-based MBSNs have attracted increased attention in recent works. In details, the Infrared (IR) communication has already been used in hospitals for tetherless communication between body sensors and monitoring equipment. In this regard, some standards has been also established for the mobile IR devices placed next to the patient in static Line-of-Sight (LoS) configurations [17]. On the other hand, when designing an OWC system, the IR transmitters and non-coherent light sources such as LEDs must conform to eye safety standards [18, 19]. In [20], common challenges of the wireless MBSNs system were reviewed. For example, energy efficiency was discussed as a significant challenge since the wireless communication is the most power consuming part of the MBSNs. Further, the presence of body in the system degrades the channel

performance, and hence modeling realistic channels which consider the complex body structure, and its movement were also introduced as one of the key challenges. It should be especially noted that [20] focused on the general overview rather than the comprehensive channel modeling. Besides, the existing wireless MBSNs communication systems in literature are based on the RF, acoustic, and long wave magnetic signals which is subjected to IEEE 1902.1.

Despite the increased attention on OWC-based MBSNs, there is a lack of relevant channel models that are specifically applicable to the OWC-based MBSNs. This lacuna of accurate channel-models is indeed a serious concern since channel modeling is the very first step for efficient, reliable, and robust link design/link enhancement. Existing deterministic [21–28] and stochastic [29–32] IR channel models are utilized for the modeling of uplink channels, while deterministic [33–40] and stochastic [41–47] VLC channel models are advantageous for modeling downlink channels in OWC-based MBSNs.

Since IR channel models have already laid the groundwork for VLC channel models, this paper starts with an overview of uplink IR MBSNs channel modeling [48–58]. Both deterministic recursive method [48–52] and stochastic Monte Carlo Ray Tracing (MCRT) models [54–58] are utilized to obtain IR channel models. Earlier studies on IR-based MBSNs mostly focused on simplistic scenarios where an ideal Lambertian source is considered, and the effects of photodetector carrying body and room equipment are neglected [48–52]. In [50], a simple dynamic LoS channel was modeled. Further, in [52], an uplink Multiple-Input Single-Output (MISO) IR channel model was established using Zero Cross Correlation (ZCC)-based Optical Code-Division Multiple-Access (OCDMA). In [53], for an alternative modulation scheme namely, the Non-Return-to-Zero-Alternate Mark Inversion (NRZ-AMI), experimental validation was presented for its improved performance compared to conventional NRZ-On Off Keying (OOK) against the IR light interference. The multiple access uplink IR scenarios were considered as Single-Input Multiple-Output (SIMO) IR scheme in [54–58]. The shadowing effect of the transmitter carrying body was considered in [57, 58].

It should be noted that the IR transmitters operate on a single optical frequency whereas the common white VL source is inherently polychromatic. Since the reflectance of most materials vary according to the wavelength of reflected signals, VLC channel models that use polychromatic light sources are much more complex than the corresponding IR channels. In this context, the IR channel models cannot be adopted in a straightforward manner for VLC channel modeling.

Earlier studies on VLC-based MBSNs [59–65] mostly focused on idealistic scenarios where fixed Lambertian reflectance is considered, and the photodetector carrying body and room equipment are neglected [59,60]. An experimental model for the simplest LoS channel was derived in [59]. Further, body presence modeling in 2D and 3D was presented in [61]. In [62], room equipment and fixed non-Lambertian reflectance were considered. The multiple access downlink VLC scenarios were considered as MISO scheme in [60–62]. Moreover, [64] considered SIMO IR scheme and MISO VLC scheme together. Furthermore, the impact of shadowing on both links, and power optimization at required QoS were investigated in [65].

This thesis is organized as follows. Chapter 2 reviews the existing IR-based MBSNs channel models in Section 2.1 and VLC-based MBSNs channel models in Section 2.2 comprehensively. Chapter 3 presents the site-specific MBSNs channel modeling, optical characterization of human skin, the methodology, and VLC-based channel modelling and characterization in various MBSNs scenarios in Sections 3.1–3.4. Chapter 4 presents the approach for the generation of random trajectories in Section 4.1 and in Section 4.2 the simulation results for scenarios on which extensive amount of trajectories implemented are demonstrated. The future research directions for VLC-based MBSN channel modeling are outlined in Chapter 5. Finally, conclusions are drawn in Chapter 6.

Chapter 2

Literature Survey

2.1 IR-based MBSNs Channel Models

In previous section, we introduced OWC-based MBSNs technology. In this section, we overview the existing IR-based MBSNs channel models [48–58] which are modelled by the deterministic recursive method [48–52], or by stochastic MCRT approach [54–58]. These models are summarized in Table 2.1. It is also worth mentioning that the optical channels are characterized by optical channel DC gain H_0 and temporal time dispersion of the channel τ_0. However, the narrowband flat fading channels with low data rates (i.e., lower than 10 Mbps) [65] and high QoS (i.e., low outage probability) [66] are established for MBSNs applications where the effect of Inter Symbol Interference (ISI) is negligible. Therefore, the optical channel models for MBSNs can be characterized by the statistical distribution of channel DC gain [2].

In [48], the diffuse IR wireless channel for a mobile patient whose mobility was statistically modelled in 2D and 3D inside a room with dimensions of 3 m × 4 m × 2.5 m is modelled by using deterministic recursive approach [22]. In this approach, the multiple reflection Channel Impulse Response (CIR) was obtained through two sequential stages. In the first stage, the reflective surfaces are assumed as purely Lambertian surfaces and then discretized into tiny surface elements. Each

tiny reflecting element with an area dA and reflectivity ρ is considered as a receiver with an area dA and received power dP. In the next stage, each of these tiny receivers is considered as a power source and the total received power at the Photodetector (PD) is then computed by collecting the contributions of each of these reflective elements. In this approach, the CIR of a single ray with an arbitrary number of reflections is computed recursively and then, the overall CIR is obtained by the summation of CIRs of each ray emitted from the light source. The light source $S = \{\mathbf{r}_S, \hat{\mathbf{n}}_S, m\}$ is described with three parameters, i.e., the arbitrary source position $\mathbf{r}_S$, source orientation $\hat{\mathbf{n}}_S$, and the Lambertian order of m. Moreover, the receiver $R = \{\mathbf{r}_R, \hat{\mathbf{n}}_R, A_R, FOV\}$ is described by four parameters, i.e., the arbitrary position of the receiver $\mathbf{r}_R$, receiver orientation $\hat{\mathbf{n}}_R$, detector area A_R, and the field of view FOV. The multiple bounce CIR therefore can be obtained as (2.1) where k is the reflection order; N is the total number of reflective elements; ε_i is the ith reflective element; ρ_i is the reflectivity of ith reflective element; α is the irradiance angle; β is the incident angle; d is the distance between the source and the receiver; c is the speed of light; and ΔA is the area of reflective element.

Besides, $\hat{\mathbf{n}}$ denotes the normal to the surface at location $\mathbf{r}$, $\otimes$ indicates the convolution, and $\text{rect}(\xi)$ is defined as

$$
\text{rect}(\xi) = \begin{cases} 0 & |\xi| > 1 \ , \\ 1 & |\xi| \leq 1 \ . \end{cases} \tag{2.2}
$$

Tracing of a single ray in deterministic recursive approach is shown in Fig. 2.1. Although this recursive method allows obtaining the overall CIR for multiple

$$
h^{(k)}(t; S, R) \approx \sum_{i=1}^{N} h^{(0)}(t; S, \varepsilon_i) \otimes h^{(k-1)}(t; \varepsilon_i, R) =
$$

$$
\frac{m+1}{2\pi} \sum_{i=1}^{N} \frac{\rho_i \cos^n(\alpha) \cos(\beta)}{d^2} \text{rect}\left(\frac{2\beta}{\pi}\right) h^{(k-1)}\left(\frac{t - d_i}{c}; \{\mathbf{r}, \hat{\mathbf{n}}, 1\}, R\right) \Delta A \tag{2.1}
$$
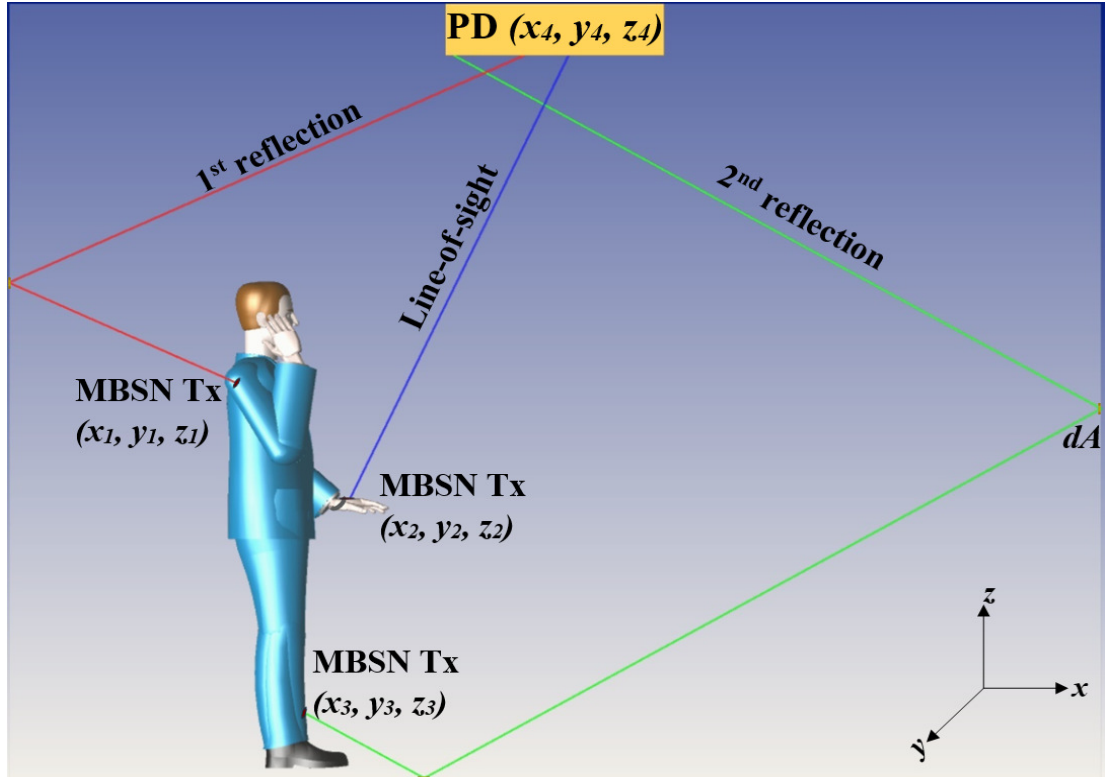
Figure 2.1: Recursive approach for MBSNs channel modeling

bounce for any order, if $k > 3$ the computation duration and computer memory requirements will increase drastically. For this reason, first order reflection from floor was considered in [48]. Besides, the scenario in [48] was built upon some simplifying assumptions such as empty room, purely Lambertian reflection, fixed reflectance values and ideal Lambertian source.

In [49], both LoS and Non-Line-of-Sight (NLoS) IR wireless channels were modelled by recursive method for a mobile patient whose 3D location was modelled by Gaussian distribution inside a room with dimensions of 3 m × 4 m × 2.5 m. The scenario in [49] was built upon some simplifying assumptions such as empty room, purely Lambertian reflection, fixed reflectance values and ideal Lambertian source.

In [50], LoS IR wireless channel was modelled by recursive method for a mobile patient whose location was modelled in both 2D and 3D by uniform and Gaussian distributions inside a room with dimensions of 3 m × 4 m × 2.5 m.

Table 2.1: Comparison table of studies on uplink IR-based MBSNs channel models

	Method	Modeling of Reflectance	Number of Reflections	Other Assumptions
[48]	Recursive algorithm	Fixed reflectance	First order	-Purely Lambertian -Empty room -Ideal Lambertian source
[49]	Recursive algorithm	Fixed reflectance	First order	-Purely Lambertian -Empty room -Ideal Lambertian source
[50]	Recursive algorithm	N/A (LoS)	No reflection	-Empty room -Ideal Lambertian source
[51]	Recursive algorithm	Fixed reflectance	First order	-Purely Lambertian -Empty room -Ideal Lambertian source
[52]	Recursive algorithm	Fixed reflectance	First order	-Purely Lambertian -Empty room -Ideal Lambertian source -MISO IR scheme
[53]	Experiment	Fixed reflectance	First order	-Purely Lambertian -Empty room -Non-ideal Lambertian source
[54]	Monte Carlo ray tracing algorithm	Fixed reflectance	Third order	-Purely Lambertian -Empty room -Non-ideal Lambertian source -SIMO IR scheme
[55]	Monte Carlo ray tracing algorithm	Fixed reflectance	Third order	-Purely Lambertian -Empty room -Non-ideal Lambertian source -SIMO IR scheme
[56]	Monte Carlo ray tracing algorithm	Fixed reflectance	Third order	-Purely Lambertian -Empty room -Non-ideal Lambertian source -SIMO IR scheme
[57]	Monte Carlo ray tracing algorithm	Fixed reflectance	Third order	-Purely Lambertian -Empty room -Non-ideal Lambertian source -3D human body and robotic platform models -SIMO IR scheme
[58]	Monte Carlo ray tracing algorithm	Fixed reflectance	Third order	-Purely Lambertian -Empty room -Ideal Lambertian source -3D human body model -SIMO IR scheme

Assuming perfect alignment between transmitter and receiver, the Probability Density Function (PDF) of channel gain, achievable data rate R_b, and minimum possible transmission power P were obtained. The results in [50] revealed that more precise channel models can be obtained where the location is modelled in 2D by Gaussian distribution. The scenario in this work was built upon some simplifying assumptions such as empty room, purely Lambertian reflection, fixed reflectance values and ideal Lambertian source.

In [51], LoS with perfect alignment and misalignment, and diffuse IR wireless channels were modelled by recursive method for a mobile patient whose location was modelled in both 2D and 3D by uniform and Gaussian distributions inside a room with dimensions of 3 m $\times$ 4 m $\times$ 2.5 m. The scenario in this work was built upon some simplifying assumptions such as empty room, purely Lambertian reflection, fixed reflectance values and ideal Lambertian source. The PDF of channel gain for these three different configurations was obtained and it was observed that the highest channel gain appears in LoS with perfect alignment scheme as expected. It was also observed that in the misaligned LoS and diffuse links the corresponding curves shift in the direction of lower channel gain values due to loss of some reflected rays which degrades the received power. The results in [51] also revealed that the misalignment angle range must be restricted within $[0°, 30°]$ to ensure desired QoS levels while this would restrict the possible mobility scenarios.

In [52], LoS and single bounce NLoS IR wireless channels were modelled by recursive method for a patient with 2D and 3D mobility in an empty room with dimensions of 4 m $\times$ 4 m $\times$ 3 m. The scenario in this work built upon some simplifying assumptions such as empty room, purely Lambertian reflection, fixed reflectance values and ideal Lambertian source. Multiple medical sensors coupled with transmitters on patient's body were considered where each node communicates with PD on the ceiling as uplinks. OptiSystem® software was utilized to compute the received power whereas Matlab® was used to model the channel and patient mobility. The PDF of channel gain for both 2D and 3D mobility in

LoS and single bounce channels were obtained and the results showed that the NLoS channel is more spread than that of LoS. The maximum possible number of medical nodes was also investigated by differentiating these nodes with OCDMA based on ZCC code, for a given QoS.

The work in [53] presented experimentally the mitigation of ambient light interference on a mobile diffuse IR channel. A low-cost commercial IR-LED at 850 nm with a power of 350 mW was used as a transmitter in a laboratory environment with dimensions 3 m $\times$ 3 m $\times$ 3 m. The receiver was fixed on the ceiling centre and the location of the transmitter on the body was modelled randomly in 2D with a fixed height of 1.4 m. A surface with a fixed Lambertian reflectivity of 0.7 was placed 1.4 m further from the transmitter which can be considered as a single floor bounce model. The detector was also placed 3 m further from the same reflective surface where 25 equally distributed transmitter locations on the 3 m $\times$ 3 m floor area were also considered. The authors then proposed a DC balanced bipolar coding, i.e., NRZ-AMI line coding, to overcome the noise and significant improvements in the BER performance were reported using the channel models.

In [54], a ray tracing channel simulator was proposed which accounts for the transmitter/receiver position, orientation, directivity, Field of View (FOV) and surface area as the IR channel modeling components. The simulation results were also verified by experiments. In the experimental setup, a triaxial accelerometer was integrated into a wearable device on patient's arm. A high-power IR diode (TSAL5100) at 940 nm was chosen as the transmitter and four receivers with FOV of 45° were fixed on the ceiling of a furnished room with dimensions of 6.6 m $\times$ 6.7 m $\times$ 3 m. The experimental results indicated that the packet loss decreases while the number of receivers increases.

In [55], MCRT simulations that consider third order reflections were verified with experimental results. In the simulations, the location of mobile patient wearing the transmitter on the arm was modelled by uniform distribution. In the experimental setup, a wearable accelerometer-based device was placed on the

patient's arm. TSAL5100 and TSAL7600 optical transmitters with half power angles $\varphi_{1/2} = 10°$ and $\varphi_{1/2} = 30°$, respectively, were considered as transmitter and four identical IR receivers were fixed on the ceiling of a room with dimensions of 6.6 m × 6.7 m × 2.5 m. The PDF of channel gain was then obtained for single active receiver scenario at $\varphi_{1/2} = 10°$ and $\varphi_{1/2} = 30°$. Both experimental packet loss values and theoretical PDF of channel gain showed that IR transmitter with $\varphi_{1/2} = 30°$ outperforms that with $\varphi_{1/2} = 10°$. It was also observed that the packet loss decreases while the number of active receivers increases.

In [56], an IR uplink communication between a transmitter located on the mobile patient and fixed four receivers with various orientations located on the ceiling of an empty room with dimension of 6.7 m × 6.6 m × 3 m was investigated. Uniformly distributed transmitter locations were considered with 10^4 points, with 10^4 links for each receiver. The Switching Combining (SwC) technique was also utilized for diversity. The CDF of channel gain for double, triple, and quadruple active receivers with orientation angles of 45° and 90° were presented. The results revealed that increasing number of the receivers with an orientation angle 45° improves the channel performance. It was also observed that the panel receivers oriented at 45° offer a better channel performance than the perpendicular oriented one because the former one can collect more reflected lights. An experiment was also presented for the same room for validation of the theoretical results. The experimental results showed that for receivers with parallel orientation, a diffused transmitter would establish a channel with higher reliability. On the other hand, if the panel receivers are perpendicularly oriented, then a collimated transmitter is a better option for modeling a channel with higher bandwidth due to the minimization of collected rays with high-order reflections.

In [57], MCRT simulations with third order reflections were verified with experimental results for an empty room with dimensions of 6.7 m × 6.6 m × 3 m. A rectangular-shaped human body as well as a robotic platform in 3D with a fixed Lambertian reflectance value were modelled to address the body impact on realistic channel modeling. Four active receivers with 45° orientation were located at

the corners of the square panel lighting that is fixed on the ceiling center. The patient location was also distributed uniformly among 10^4 points on 2D plane. The CDF of channel gain for various transmitter heights of $h = 0.15, 0.22, 0.5, 0.9, 1.2, 1.5$, and 1.7 m were presented in the absence and presence of the human body. The results in [57] revealed that the channel performance degrades significantly when the transmitter height is less than 1.2 m due to the blockage of the human body.

In [58], an uplink IR communication between a randomly orienting transmitter located on the mobile patient's wrist and fixed four receivers with 45° orientation placed on the ceiling in an empty room with a dimension of 6.7 m × 6.6 m × 3 m was investigated. Different gait patterns corresponding to a young person and an old person are considered in the Random Walk (RW) model. The Lambertian reflectivity of the room surfaces and 3D human bodies are considered as 0.8 and 0.1, respectively. A Lambertian source is taken into consideration in MCRT simulations with three reflections. According to the simulation results, the channel gain is overestimated if the simulation results of a young person who walks upright are considered rather than those of a humpbacked older person when designing an IR-based MBSNs system for an elder. However, selecting any of these bodies leads to an insignificant impact on the channel selectivity.

While earlier works in [48–58] discussed uplink IR-based MBSNs channel models, there are some works on node-to-node (i.e., on-body) MBSNs channel models [67–71]. In [67, 68], a static on-body IR-based MBSNs channel models were investigated. In [67], stochastic MCRT method was used whereas deterministic single bounce recursive method was adopted in [68]. Idealistic assumptions such as ideal Lambertian source and fixed reflectance values were considered in these works and ideal wavelength-independent sources were considered. In [69], deterministic one bounce recursive model was adapted to model a mobile on-body IR channel in a diffuse configuration. In [70], a mobile on-body IR channel with MISO scheme was modelled in a diffuse configuration where the differentiation

between the signals of each transmitter nodes was established by utilizing unipolar Optical Orthogonal Code (OOC)-based OCDMA. In [71], a mobile on-body IR channel was modelled in a diffuse configuration. Ten on-body sensors coupled with transmitters communicate with two coordinator nodes coupled with receivers placed on the hip and the shoulder while 3D body moves in a realistic walk cycle. The non-sequential MCRT algorithm with $k = 3$ was adopted which allows to create realistic environment. Patient random mobility was also modelled with modified Random Waypoint (RWP) model. The optical channel DC gain, Root Mean Square (RMS) delay spread, and coherence time features were obtained to characterize the channels between the transmitter sensor nodes and receiver coordinator nodes in local and global mobility scenarios.

2.2 VLC-based MBSNs Channel Models

In Section 2.1, the existing IR-based MBSNs channel models are discussed [48–58]. In this section, we overview the existing VLC-based MBSNs channel models [59–65] which are summarized in Table 2.2. In terms of the mobility of the corresponding transmission component, these works can be categorized into static and dynamic channel models. It should be noted that both unidirectional and bidirectional communication modes have been considered in existing dynamic channels.

2.2.1 Static Channel Models

In [59], the static LoS downlink VLC channel was experimentally established where the location of the transmitter and receiver are fixed with LoS distance 0.5 m. The NRZ-OOK modulation was used with a carrier frequency of 100 kHz to not disturb the human eye while both illuminating and transmitting data. The results showed that a maximum data rate of 56 kbps is achieved for targeted $BER = 10^{-6}$.

13

In [72–75], the static LoS uplink VLC-based MBSNs channel model were experimentally investigated. In [72], an active IR and passive VLC transmission was considered where a Thin-film Corner Cube Retroreflector (TCCR) was employed as a rechargeable battery to modulate and reflect the measurements from the sensors on the body. In [73, 74], multiple sensors were used and the data was sent as a single combined signal by a VLC transmitter to a receiver. In [75], the Optical Camera Communication (OCC) was utilized in a MBSNs system. In [67, 68], a static on-body IR-based MBSNs channel models were investigated. In [67], stochastic MCRT method was used whereas deterministic single bounce recursive method was adopted in [68]. Idealistic assumptions such as ideal Lambertian source and fixed reflectance values were considered in these works and ideal wavelength-independent sources were considered.

2.2.2 Mobile Channel Models

In previous subsection, we overviewed the existing static VLC-based MBSNs channel models. In this subsection, we overview the existing dynamic VLC-based MBSNs channel models where both unidirectional [60–62] and bidirectional [63–65] channel models are considered.

In [60], the stochastic MCRT method was adopted for CIR modeling with $k = 1, 3$, and 7 reflections inside an empty room with dimensions of $5\,\text{m} \times 5\,\text{m} \times 3\,\text{m}$ where four VLC transmitters are placed on the ceiling. Two different mobility scenarios were considered while the patient who wears the receiver walks around the room. In the first scenario, the axes of the receiver location were modelled with a uniform distribution on 2D plane. In the second scenario, the random orientation of the receiver induced by the patient's body movements were modelled according to a uniform distribution. The results revealed that when the elevation and azimuth angles are equal to $\pi/3$, the impact of the NLoS rays on CIR are more pronounced than that of the LoS rays. Therefore, to obtain a more accurate delay spread and ISI information, the CIR with $k = 7$ is needed. On the other hand, when the

orientation angle are equal to 0, or perpendicular, the impact of the LoS rays on CIR are more pronounced than that of the reflected rays, i.e., the higher order of reflections does not contribute much in the CIR. The results in [60] also revealed that the effect of receiver orientation does not imply significantly on the channel model performance for the data rates up to 30 Mbps.

In [61], the stochastic MCRT method with $k = 3$ was adopted for the same environment of [60] where double mobility model for the receiver location and orientation was considered. As for the human body modeling, two different models were investigated, i.e., 2D generic body model with dimensions 1.72 m × 0.45 m and highly detailed 3D mesh body model where a thickness of 0.25 m with 1796 facet was integrated into the model. The surface reflection of 2D and 3D bodies were also modelled as purely Lambertian Bidirectional Reflectance Distribution Function (BRDF) with a fixed reflectance value ρ. The optical channel DC gain was obtained for scenarios with (i) absence of the body, (ii) presence of the 2D body with $\rho = 0.7$, (iii) presence of the 3D body with $\rho = 0.7$, (iv) presence of the 2D body with $\rho = 0.1$, and (v) presence of the 3D body with $\rho = 0.1$. The results reveal that a simplistic 2D body model is sufficient for channel modeling if the body reflection is high. Besides, it was observed that the reflectivity is more important than the level of details while modeling a human body.

In [62], the impacts of the physical and geometrical parameters on channel modeling were investigated. An empty room with dimensions of 5 m × 5 m × 3 m was considered where the transmitter oriented towards the floor was fixed on the ceiling and modelled with a Lambertian directivity $m = 1$. The location of a mobile receiver oriented towards the ceiling was also statistically modelled in 2D plane. The coating materials were modelled by purely diffusive (Lambertian), or mixed (Blinn-Phong) models. Six configurations were investigated in [62], i.e., (1,2) empty regular bedroom and hospital bedroom, (3,4) regular bedroom and hospital room with 2D body model and furniture, and (5,6) regular bedroom and hospital room with 3D body model and furniture. The results indicate that the impact of detail-levels supersedes compare to impact of furniture and human

Table 2.2: Comparison table of studies on downlink VLC-based MBSNs channel models

	Method	Modeling of Reflectance	Number of Reflections	Other Assumptions
[59]	Experiment	N/A (LoS)	No reflection	-Empty room -Commercial white LED
[60]	Monte Carlo ray tracing algorithm	Fixed reflectance	Seventh order	-Purely Lambertian -Empty room -Ideal Lambertian source -MISO VLC scheme
[61]	Monte Carlo ray tracing algorithm	Fixed reflectance	Third order	-Purely Lambertian -Empty room -2D and 3D human body models -Ideal Lambertian source -MISO VLC scheme
[62]	Monte Carlo ray tracing algorithm	Fixed reflectance	Third order	-Diffuse, and mixed reflections -Room with furniture -2D and 3D human body models -Ideal Lambertian source -MISO VLC scheme
[63]	Monte Carlo ray tracing algorithm	Fixed reflectance	Third order	-Purely Lambertian -Empty room -2D human body model -Ideal Lambertian source -SIMO IR scheme
[64]	Monte Carlo ray tracing algorithm	Fixed reflectance	Third order	-Purely Lambertian -Empty room -2D human body model -Ideal Lambertian source -SIMO IR scheme -MISO VLC scheme
[65]	Monte Carlo ray tracing algorithm	Fixed reflectance	Third order	-Purely Lambertian -Empty room -3D human body model -Ideal Lambertian source -SIMO IR scheme

body presence in the regular bedroom. On the contrary, the impact of furniture and body presence supersedes compare to impact of detail-levels in the hospital bedroom. It was also observed that the impact of detail-levels increases with an increase in data-rate.

In [63–65], a full-duplex bidirectional (i.e., downlink VLC and uplink IR channels) dynamic OWC-based MBSNs channel was presented where the MCRT simulations with $k = 3$ are made for modeling diffuse IR and VLC channels. As for downlink channel, an LED panel of dimensions 0.6×0.6 m was fixed on the ceiling center as an ideal Lambertian source with $m = 1$. A VLC receiver with a perpendicular orientation was also integrated into a tablet which is held in front of the moving patient at fixed height of 1.2 m. The patient location was statistically modelled among 10^4 points on 2D plane. As for uplink channel, an IR transmitter with perpendicular orientation was placed on the shoulder of the moving patient at fixed height of 1.2 m. Four identical IR receivers were also fixed at the corners of LED panel. The results in [63, 64] revealed that the channel reliability of uplink IR channel with optimal orientation is superior to that of the downlink VLC channel with the body presence. Besides, the precise modeling of human body reflectivity is indispensable for the indoor scenarios with random receiver orientation.

Chapter 3

Static Channel Modelling in Real-Life Based Hospital Scenarios

3.1 Site-Specific MBSNs Channel Modeling

In previous sections, we reviewed the existing OWC-based MBSNs channel models. In this section, we introduce the site-specific MBSNs channel modeling method using advanced non-sequential ray tracing tool of Zemax® [47, 76]. In this software, there are two modes of ray tracing. In sequential ray tracing, rays are traced through a sequence of surfaces, hitting each surface only once, while traveling from the transmitter to the receiver. This property makes sequential mode ideal for imaging systems. On the other hand, non-sequential ray tracing allows rays to propagate through environment in any order and allows rays to be scattered and reflected back to an object that they have already encountered. This property makes non-sequential mode ideal for impulse response modeling which is adopted in our study.

Our approach obtains CIRs for various indoor environments with diverse room-dimensions and assumes integration of realistic light sources in the simulation environment. Furthermore, many reflections (more than 10) can be easily handled for better accuracy including specular and mixed specular-diffuse reflections. Major steps of the proposed MBSNs channel modeling approach are illustrated in Fig. 3.1. In the first step, we create a 3D simulation environment where we can
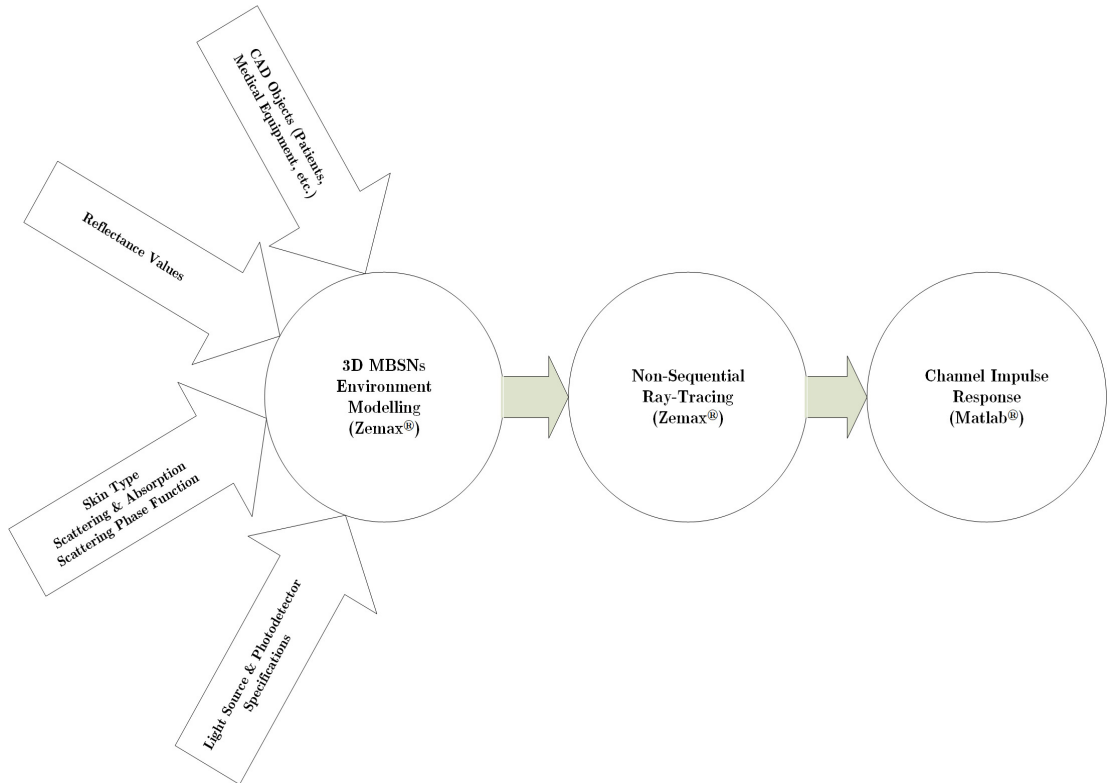
Figure 3.1: Main steps of site-specific channel modeling for VLC-based MBSNs

specify the geometry of the indoor environment, the objects within, the reflection characteristics of the surface materials, the absorption, scattering and scattering phase function of human skin, and the specifications of the light sources and detectors. In the second step, we use non-sequential ray tracing to calculate the detected power and path lengths from source to detector for each ray. In the third step, we import this data to Matlab$^{\text{®}}$ and obtain the CIRs for the considered scenario.

3.2 Optical Characterization of Human Skin

The main optical characteristics of tissues in VL spectrum are the wavelength-dependent refractive index $n(\lambda)$, absorption coefficient $\mu_a(\lambda)$, scattering coefficient $\mu_s(\lambda)$, anisotropy factor $g(\lambda)$ (i.e, the average cosine of scattering angle in all scattering directions), and scattering phase function [79]. Water makes up the large part of the most tissues and it has the minimum refractive index among

19
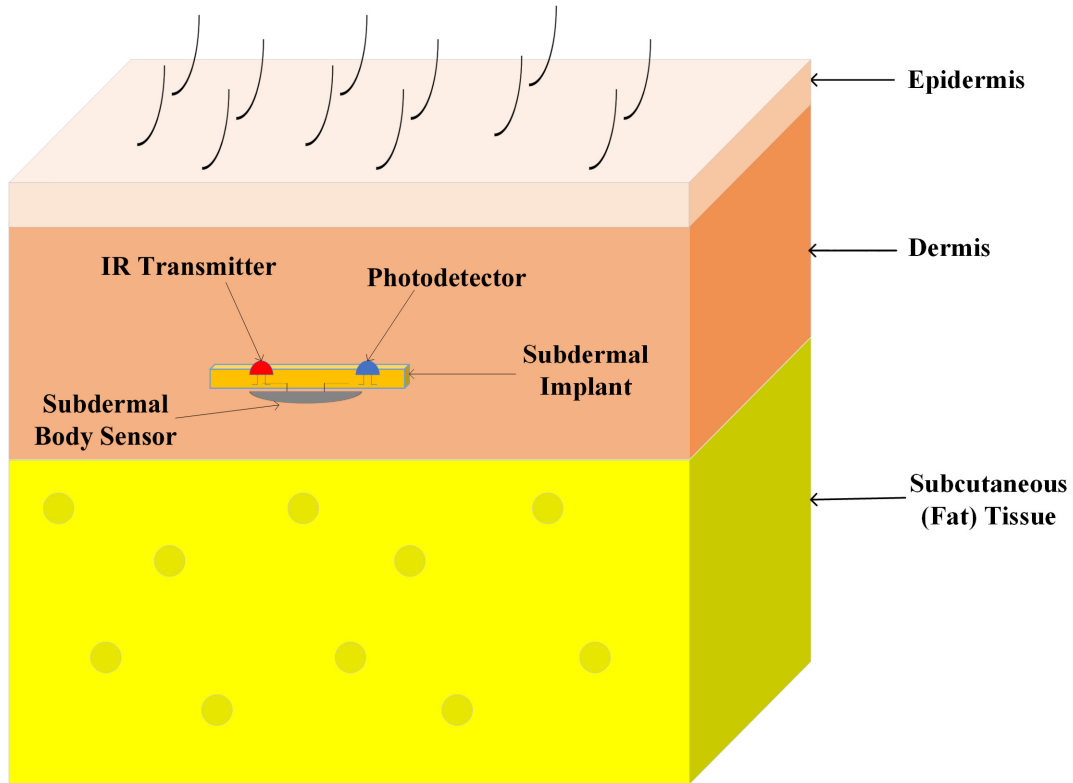
Figure 3.2: Subdermal sensor placement in conventional three-layered skin model

all tissue components. Moreover, water is measured as the dominant absorption molecule in IR spectrum whereas hemoglobin and melanin are the dominant ones in VL range. The most appropriate frequency range to mitigate the absorption effects is between the red to near-IR spectrum, i.e., 600-1300 nm and called as the diagnostic and therapeutic window. Experiments have been also conducted on ex-vivo human skin using Monte-Carlo inversion technique in [80]. Integrating sphere has been used for the reflectance and transmittance measurements by sending collimated beam in wavelengths between 620 to 1000 nm. The absorption and scattering coefficients depending on these wavelengths are obtained for dermis, fat, and muscle layers of the skin. It is observed that the absorption coefficient decreases while the wavelength is increasing until 825 nm. Then, it starts to rise until 1000 nm. On the other hand, scattering coefficient shows a gradual reduction while the wavelength is increasing. The experiment results in [80] also show that the skin tissue comprising epidermis, dermis, and fat layers with 11.5 mm thickness allows significant power transmission.
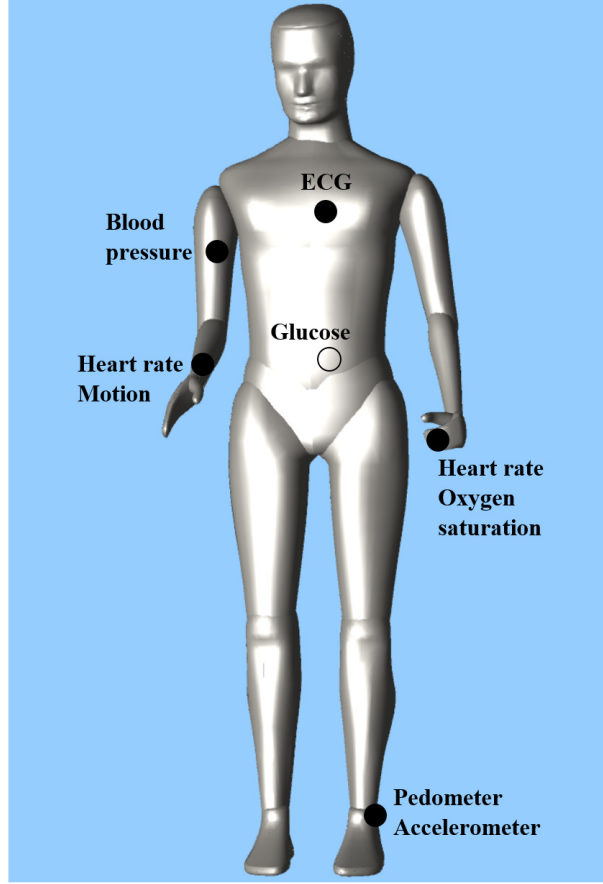
Figure 3.3: Typical MBSN node locations

For most biological tissues, the anisotropy factor is approximately 0.9 which corresponds to anisotropic forward scattering. There are also some other key factors determining the quality of Transdermal Communication (TC) channel between the implanted transceiver and on-body transceiver (see Fig. 3.2) such as the skin tissue thickness, the size of the integration area of the optics, optics system efficiency factor, the amount of misalignment, and the transmitter power [81].

To model scattering phase function, One-Term Henyey-Greenstein (OTHG) scattering phase function $P(\vartheta)$ fits well when approximating the human skin [82]. It is described by only a single parameter, i.e., the anisotropy factor, as [83]

$$P(\vartheta) = \frac{1}{4\pi} \frac{1 - g^2}{\left(1 + g^2 - 2g\,\cos\vartheta\right)^{3/2}} \tag{3.1}$$

where ϑ is the longitudinal scattering angle.

Table 3.1: MBSNs applications

Clinical applications	Sensor location	Sensor types
Glucose home monitoring	Subcutaneous	Glucose
	Eye	Glucose
	Arm	Multi-variable
Cardiopulmonary and vascular monitoring	Wrist	Ultrasound
		Multi-variable
		Photoplethysmograph (PPG)
		Electrocardiograph (ECG)
	Finger (ring sensor)	Optical (heart rate)
		Radio-frequency identification
	Arm or thigh	Microwave reflectometric cardiopulmonary
	Compatible with various equipment	Optical sensor
		ECG electrodes
	Phone adapter	Single-channel ECG
	Seat belt of a car	Wired strain gauge
Neurological function monitoring	Clothes	Inertial sensors Accelerometers
	Visual feedback-glasses	Inertia
	Auditory feedback-headphones	
	Wrist or ankle	Accelerometer Motion
Physical therapy and rehabilitation	Ankle	Pedometers Accelerometer

Medical body sensors are also categorized based on their locations (see Fig. 3.3), usage areas, and clinical applications [84] (see Table 3.1). For example, subcutaneous sensors measuring the glucose level in the body are used in glucose home monitoring applications.

There are also conventional skin models in the literature, i.e., three-layered skin model [77] which comprises epidermis, dermis, and subcutaneous tissues; seven-layered [78] and nine-layered [77] skin models. The multilayered skin models are detailed in Table 3.2. The absorption and scattering coefficients of three-layered

Table 3.2: Various multilayered skin models

Three-layered model [77]	Seven-layered model [78]	Nine-layered model [77]
Epidermis (Blood-free layer)	Stratum corneum	Stratum corneum
	Living epidermis	Stratum granulosum, Stratum spinosum
		Stratum basale
Dermis (Vascularized layer)	Papillary dermis	Papillary dermis
		Subpapillary dermis
	Upper blood net dermis	Upper blood net dermis
	Reticular dermis	Reticular dermis
	Deep blood net dermis	Deep blood net dermis
Subcutaneous tissue (Fat layer)	Subcutaneous tissue	Subcutaneous tissue

model are presented in Figs. 3.4 and 3.5 [85].

Based on the key factors described above, the received power in TC channel is calculated as

$$P_r = \int_A P \, J_{Rx\lambda} \, \eta_\lambda \, dA \qquad (3.2)$$

where P is optical transmitted power, $J_{Rx\lambda}$ is spatial optical power distribution on the skin at wavelength λ, η_λ is the efficiency factor, and A is the tissue area.

3.3 Methodology

Based on Table 2.1 and 2.2, it is inferred that MCRT is widely used in the literature as a more flexible tool for channel modeling. This statistical method can determine the channel characteristics by generating numerous photons and then simulating the interactions of each photon with the medium. The MCRT allows importing the key parameters of TC channel such as refractive index, absorption coefficient, scattering coefficient, and scattering phase function. The refractive index determines the photon reflection and refraction at Fresnel boundaries between the tissue layers which defines the speed of light within the tissue and

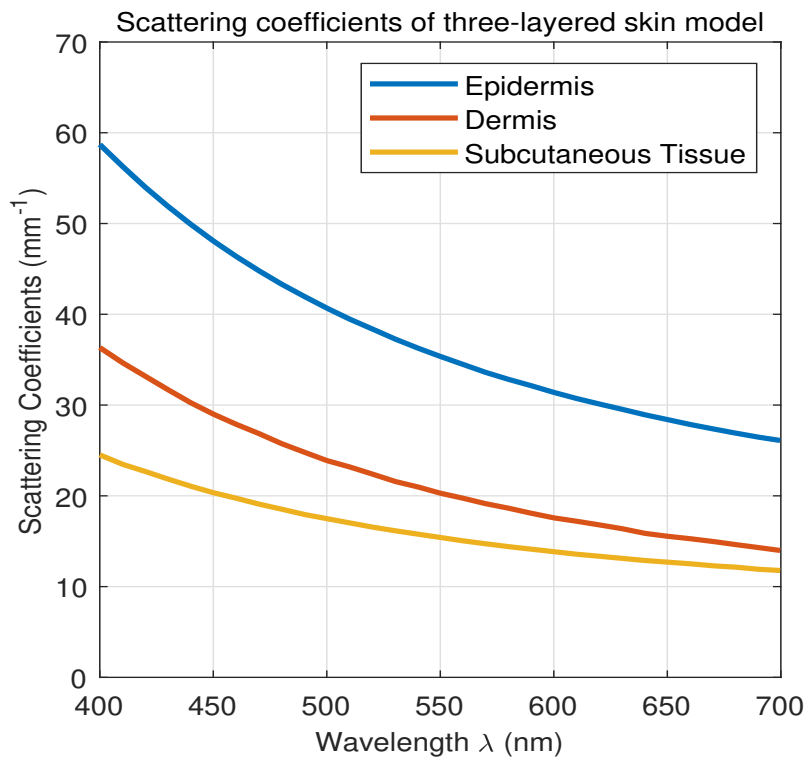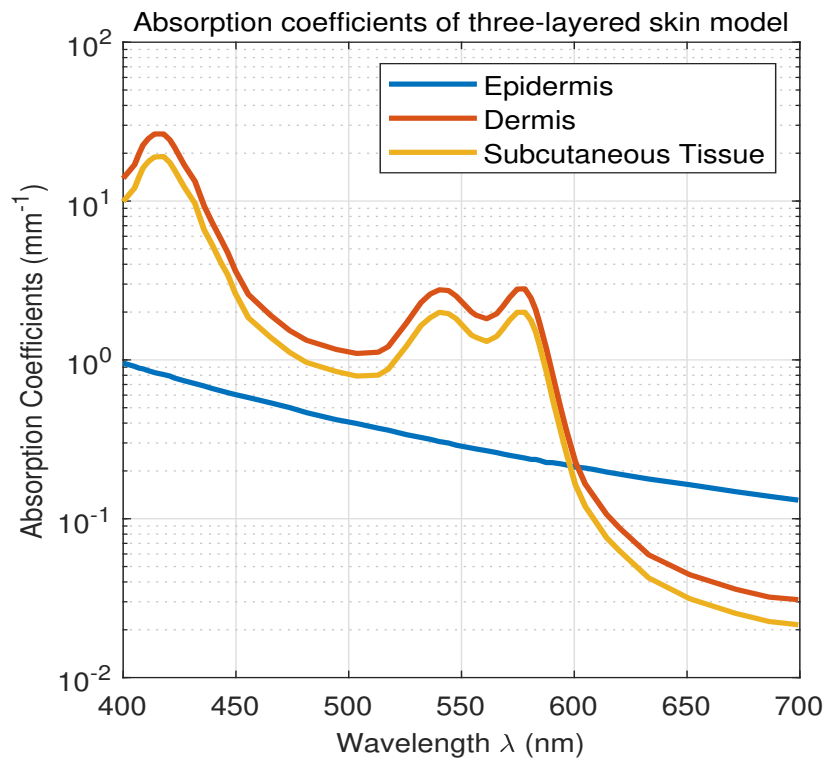Figure 3.4: Absorption and scattering coefficients of human skin in three-layered skin model [85] for VL band. Top: Absorption coefficient of human skin. Bottom: Scattering coefficient of human skin.
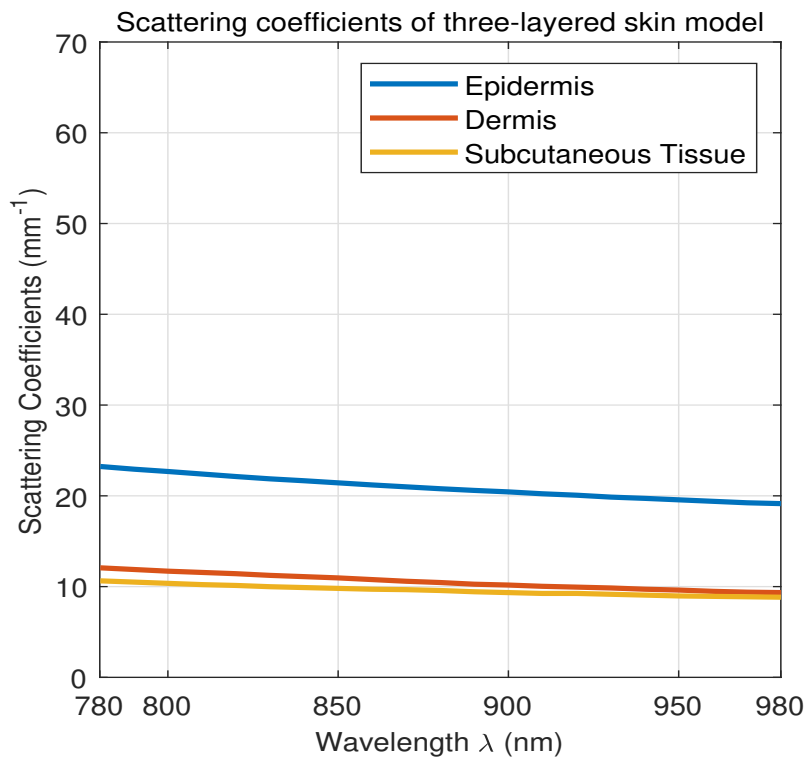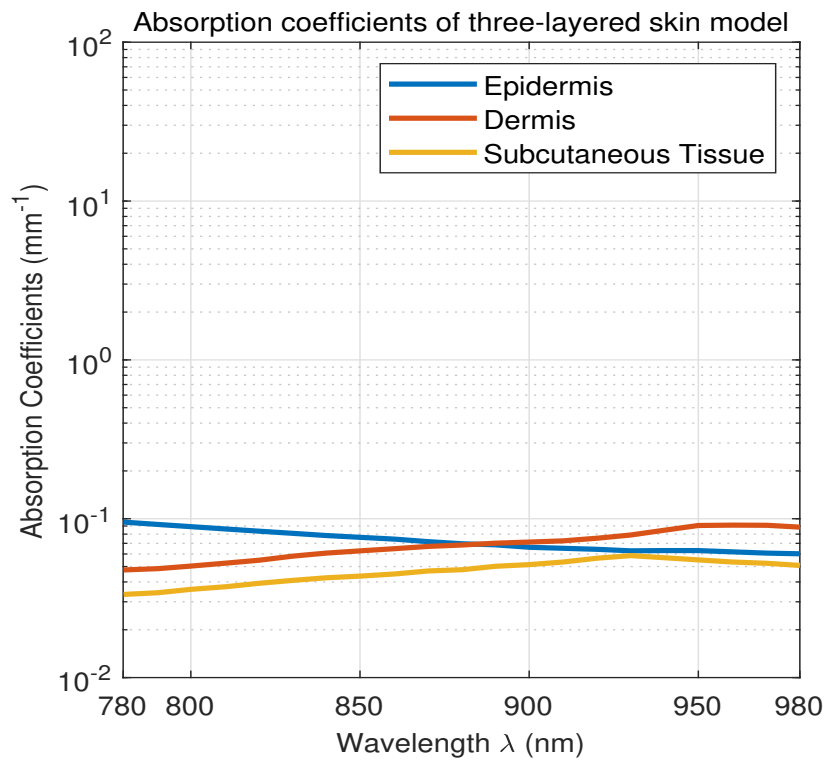
Figure 3.5: Absorption and scattering coefficients of human skin in three-layered skin model [85] for IR band. Top: Absorption coefficient of human skin. Bottom: Scattering coefficient of human skin.

Table 3.3: Simulation parameters for downlink VLC skin channel model in adopted three-layered skin model

Layers	Thickness (μm) [81]	$\bar{\mu}_a(\lambda)$ (mm^{-1}) [83]	$\bar{\mu}_s(\lambda)$ (mm^{-1}) [83]	Mean free path	Photon weight updating	n [84]	g [76]
Epidermis	$100-120$	0.3701	37.7195	0.0263	0.9903		
Dermis	$1710-2200$	3.6640	21.9560	0.0390	0.8570	1.4	0.9
Subcutaneous tissue	$6000-6500$	2.6085	16.3183	0.0528	0.8622		

Table 3.4: Simulation parameters for uplink IR skin channel model in adopted three-layered skin model

Layers	Thickness (μm) [81]	$\bar{\mu}_a(\lambda)$ (mm^{-1}) [83]	$\bar{\mu}_s(\lambda)$ (mm^{-1}) [83]	Mean free path	Photon weight updating	n [84]	g [76]
Epidermis	$100-120$	0.0730	20.9302	0.0476	0.9965		
Dermis	$1710-2200$	0.0690	10.5482	0.0942	0.9935	1.4	0.9
Subcutaneous tissue	$6000-6500$	0.0469	9.5971	0.1037	0.9951		

the manner in which photons penetrate tissue. Although the refractive index is wavelength dependant, according to the measured data reported in [80] and [86], the refractive indices of epidermis, dermis, and fat layers are set to $n = 1.4$ (see Table 3.3). The absorption and scattering coefficients define the probability of a photon to be absorbed and scattered per unit length, respectively. Based on Fig. 5, the average values of $\mu_a(\lambda)$ and $\mu_s(\lambda)$ over $400-700$ nm (i.e., the spectrum of VL source) and $780-980$ nm (i.e., the spectrum of IR source), are computed for three-layered skin model (see Tables 3.3 and 3.4).

The scattering phase function $P(\vartheta)$ defines the PDF for scattering in a direction at an angle ϑ relative to the direction of the traveling photon. In human skin modeling, OTHG scattering phase function provides the most realistic approximation [87]. The OTHG formula is modelled with three parameters which are mean free path, photon weight updating, and anisotropy factor [87]. The mean

free path which defines the average distance covered by propagating photons before a scattering event occurs is given by

$$\text{Mean Free Path} = \frac{1}{\mu_a + \mu_s} \ . \tag{3.3}$$

The photon weight updating which defines the change in weight of transmitting photon after occurrence of absorption and scattering events during its travel is given by

$$\text{Photon Weight Updating} = \frac{\mu_s}{\mu_a + \mu_s} \ . \tag{3.4}$$

The anisotropy factor defines the mean cosine of scattering angle ϑ. This parameter changes between -1 and 1 such that minus unity, zero and unity indicates total backscattering, isotropic (Rayleigh) scattering, and total forward-scattering (Mie), respectively. In biological tissues, Rayleigh scattering contributes due to small-scale structures whereas Mie scattering contributes due to collagen fibres in skin tissue [77]. The mean free path, photon weight updating, and anisotropy factor for the adopted three-layered skin model in the proposed downlink VLC and uplink IR skin channel models are summarized in Tables 3.3 and 3.4. It should be noted that there is a trade-off between skin thickness and power efficiency. Choosing an implant location with a very thin dermal covering provides a very significant power advantage [81]. In that respect, the subdermal sensor in conventional three-layered skin model is placed within dermis layer due to smaller thickness of dermis and epidermis layers. Therefore, only the refractive index of these two layers are of importance in skin tissue channel modelling.

Based on the approach summarized above, the skin channel model can be realized by considering the uplink and downlink channels separately. The thickness of epidermis and dermis layers are selected as 100 μm and 2000 μm, respectively. The implant is placed in the middle of dermis layer and hence the distance between transmitter and receiver is 1100 μm. We consider the IR and VL transmitters with the same half viewing angle of 60 degrees and the FOV and the area of the detector for both channels are 90° and 1 cm^2, respectively. A total unit
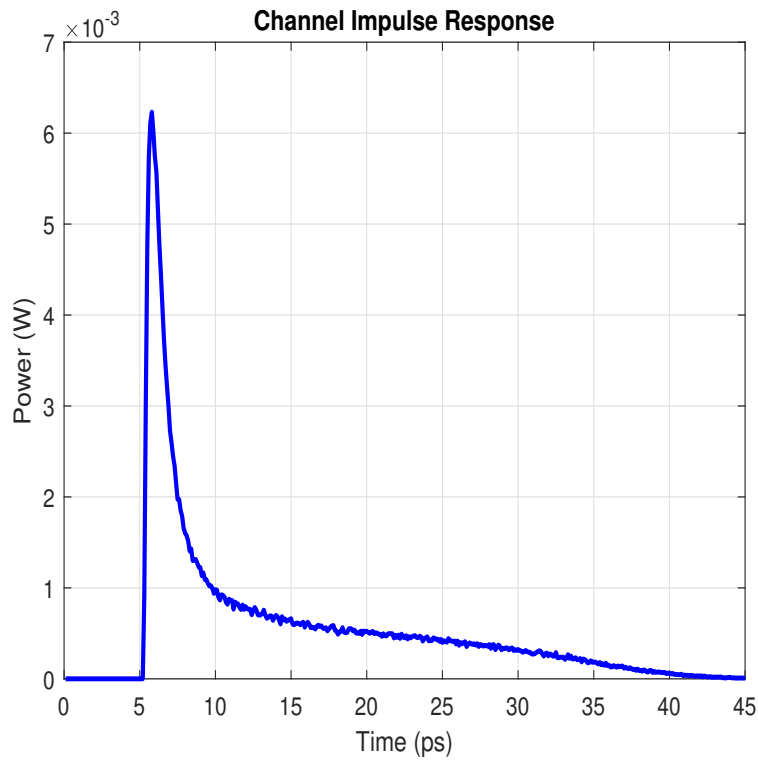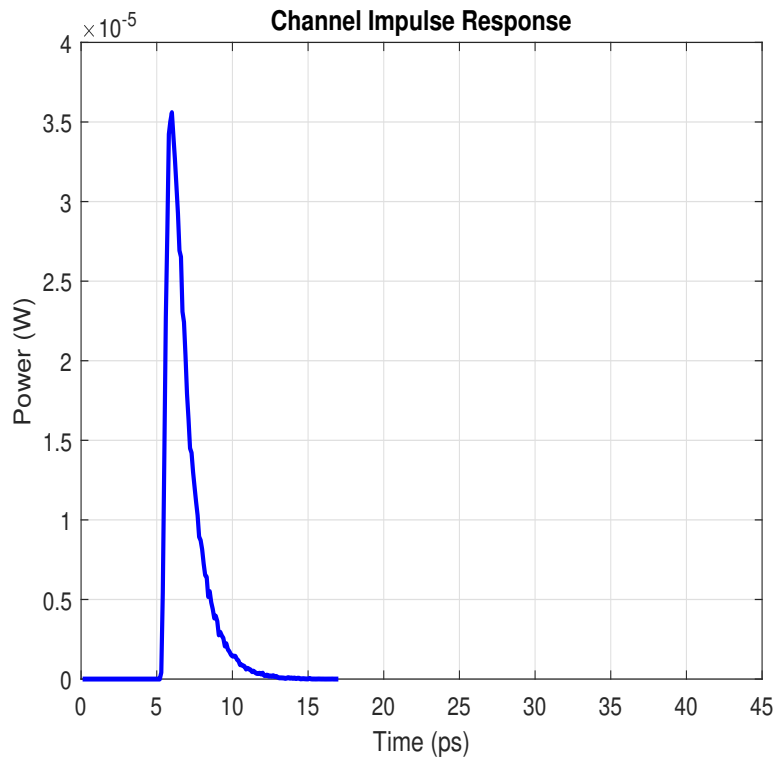
Figure 3.6: Human skin channel models. Top: Downlink VLC channel model (from epidermis to dermis). Bottom: Uplink IR channel model (from dermis to epidermis).

(normalized) power is assumed for both IR and VL transmitters. The perfect alignment configuration is considered for both uplink and downlink channels. Downlink VLC and uplink IR skin channel models obtained through the proposed site-specific MBSNs channel modeling approach are presented in Figs. 6a and 6b, respectively. It is observed that the maximum received power is 35.69 μW at 6 ps for the downlink VLC channel (i.e., from epidermis to dermis) whereas it peaks at 6.23 mW at 5.8 ps for the uplink IR channel (i.e., from dermis to epidermis). Besides, the delay spread values of the downlink VLC channel and uplink IR channel are around 10 ps and 40 ps, respectively. These discrepancies are due to this fact that the optical properties of skin tissue layers are wavelength-dependent, and the emitted rays from VL transmitter in downlink VLC channel traverses from epidermis to dermis layer while the emitted rays from IR transmitter in uplink IR channel traverses from dermis to epidermis.

3.4   Real-Life Based Hospital Scenarios

In this section, based on the proposed approach summarized in Section 3.1, we model the channels for four MBSNs reference scenarios, i.e., Intensive Care Unit (ICU) ward, clinic, semi-private patient room, and family-centered patient room (see Fig. 3.6). These scenarios are constructed as per requirements in [88] and [89]. The specifications of the reference scenarios are detailed in Table 3.5. The coating materials of objects in scenarios under consideration are summarized in Table 3.6. Next, we describe each of these scenarios accompanied with corresponding CIRs.

For predefined number of rays, the advanced ray tracing calculates the path length and detected power of each ray launched from transmitter to receiver. These are further processed in Matlab$^{\circledR}$ to obtain the CIR as follows:

$$h_{\text{VLC}}(t) = \sum_{i=1}^{N_r} P_i \ \delta(t - \tau_i),\tag{3.5}$$

Table 3.5: Specifications of scenarios under consideration

Features	ICU ward	Clinic	Semi-private patient room	Family-centered patient room
Number of beds	4	1	2	1
Number of bodies	5	3	4	3
Number of sources	15	5	8	8
Number of PDs	16	6	8	4
Dimensions (L×W×H) (m)	11.5×6.5×3	5×4×3	8.8×5×3	7×5×3
Clear floor area per bed (m^2) [88, 89]	13.69	14	14.13	23.66
Side clearance on non-transfer side of bed (m) [88]	≈ 1	≈ 1	≈ 1	≈ 1
Side clearance on transfer side of bed (m) [88]	1.5	$\gg 1.22$	2	$\gg 1.22$
Clearance at the foot of each bed (m) [88]	2.3	1.7	2.3	2.3

Table 3.6: Coating materials for the scenarios under consideration

Scenario 1 ICU ward	**walls:** plaster, **ceiling:** plaster, **floor:** pinewood, **hospital bed:** aluminium, **ICU desk:** pinewood, **chair:** black gloss paint
Scenario 2 Clinic	**walls:** plaster, **ceiling:** plaster, **floor:** pinewood, **hospital bed:** aluminium, **medical ultrasound machine:** aluminium, **desk:** pinewood, **chair:** black gloss paint, **laptop:** black gloss paint
Scenario 3 Semi-private patient room	**walls:** plaster, **ceiling:** plaster, **floor:** pinewood, **WC door:** pinewood, **curtain:** cotton, **hospital bed:** aluminium, **chair:** black gloss paint, **drawer:** pinewood, **wardrobe:** pinewood
Scenario 4 Family-centered patient room	**walls:** plaster, **ceiling:** plaster, **floor:** pinewood, **WC door:** pinewood, **hospital bed:** aluminium, **chair:** black gloss paint, **drawer:** pinewood, **wardrobe:** pinewood, **sofa cover:** cotton, **side tables:** pinewood, **coffee table:** pinewood

where P_i is the received power of the ith ray, τ_i is the propagation time of the ith ray, $\delta(t)$ is the Dirac delta function and N_r is the received number of rays.

A VLC-based MBSNs channel is characterized by the channel DC gain which is the collected portion of the launched rays, and it is expressed as:

$$H_0 = \int_0^{+\infty} h_{\text{VLC}}(t)dt. \tag{3.6}$$

Another essential channel characteristic is the RMS delay spread, which is a metric presenting the temporal dispersion of the multipath transmission, and it is defined as:

$$\tau_{RMS} = \sqrt{\frac{\int_0^{+\infty} (t - \tau_0)^2 \, h_{\text{VLC}}(t)dt}{\int_0^{+\infty} h_{\text{VLC}}(t)dt}} \tag{3.7}$$

where τ_0 is the mean delay spread.

$$\tau_0 = \int_0^{+\infty} t \, h_{\text{VLC}}(t)dt \Big/ \int_0^{+\infty} h_{\text{VLC}}(t)dt \tag{3.8}$$

3.4.1 ICU Ward

In this scenario, an ICU ward which consists of four patients laying on their beds, and a continuously working medical staff standing in front of her desk and chair, is considered (Fig. 3.7). The dimensions of ICU ward is 11.5 m $\times$ 6.5 m $\times$ 3 m where 15 luminaires are uniformly located on the ceiling. The luminaires in MBSNs reference scenarios under consideration are commercially available from Cree® 14-40LHE with a half viewing angle of 55 degrees and 125 lumens per watt efficacy. As illustrated in Fig. 3.9, the illuminance uniformity (i.e., as the ratio of the minimum illuminance to the average one), minimum, maximum and average values of illumination are calculated as 0.89, 72.93 lx, 89.71 lx, and 82.30 lx, respectively which meet the illumination requirements of ICU ward [90, 91].

Sixteen different locations are considered for PDs (D1,...,D16)[1]. A PD is located on the top side of the foot plate of each patient bed, a pair of PDs is placed on right and left inner arms of each laying patient, a PD is positioned on the wrist of the medical staff, and three PDs are placed on the corners of L-shape desk in the environment.

The sample CIRs for the scenario under consideration are shown in Figs. 3.12. It is observed from $h_{\mathrm{S_{12}D_{13}}}(t)$ that the LoS rays are dominant. This is due to the fact that the detector D13 is placed on the desk that is used by the nurse, and it stands just under the VLC source. It is also observed from $h_{\mathrm{S_{11}D_{11}}}(t)$ that the diffused rays are dominant since the detector D11 on MBSN node worn by the patient is at the opposite of the VLC source and many objects are placed between them.

3.4.2 Clinic

In this scenario, a clinic which consists of single patient laying on the bed next to the medical ultrasound device, and a medical doctor and patient's companion sitting opposite while both holding their cell phones is considered (Fig. 3.7). The dimensions of the clinic is 5 m × 4 m × 3 m where 5 luminaires are uniformly located on the ceiling. As illustrated in Fig. 3.9, the illuminance uniformity, minimum, maximum and average values of illumination are calculated as 0.78, 407.70 lx, 611.80 lx, and 521.38 lx, respectively which meet the illumination requirements of a clinic [90, 91]. Six different locations are also considered for PDs (D1,...,D6). A PD is located on the top side of the medical ultrasound device screen, a pair of PDs is placed on right and left inner arms of the laying patient, a PD is positioned on the top of each cell phone of doctor and patient's companion, and the last PD is located on top of a USB inserted to laptop computer.

---

[1]It is possible to improve signal-to-noise ratio (SNR) by narrowing the receiver FOV through the use of a proper lens. However, a narrow FOV might be problematic for mobile conditions. Therefore, we prefer a large FOV (i.e., 90 degrees) in this study to maximize reception angle.
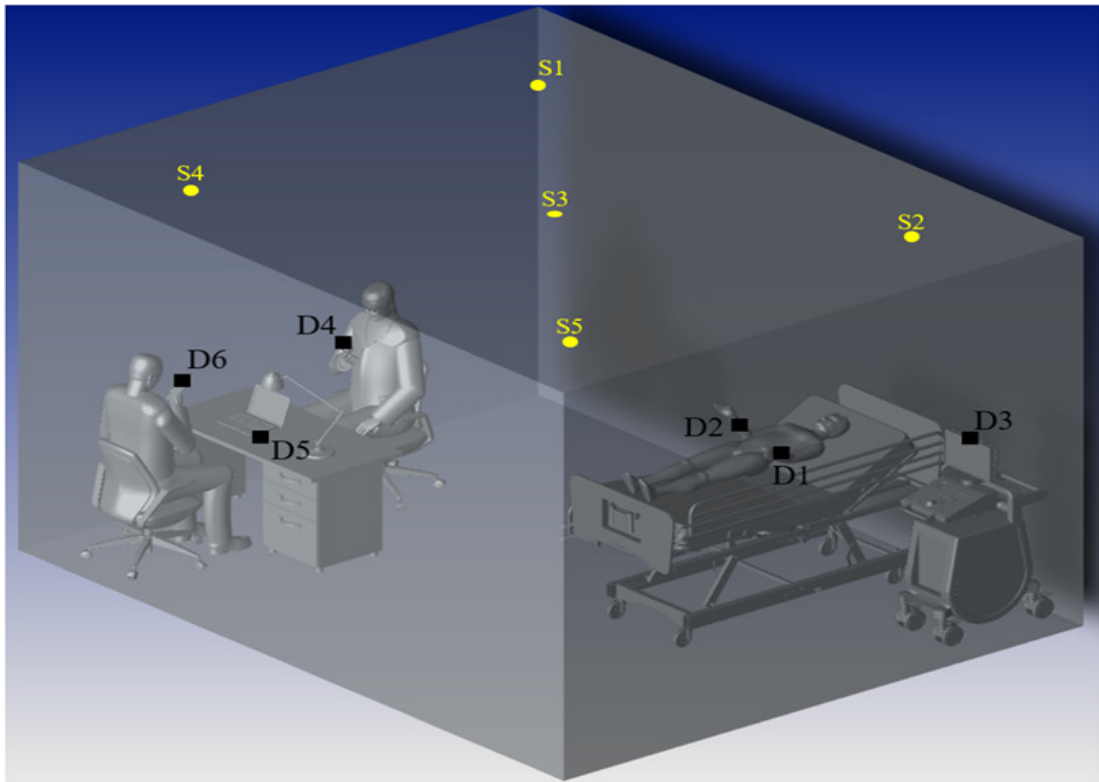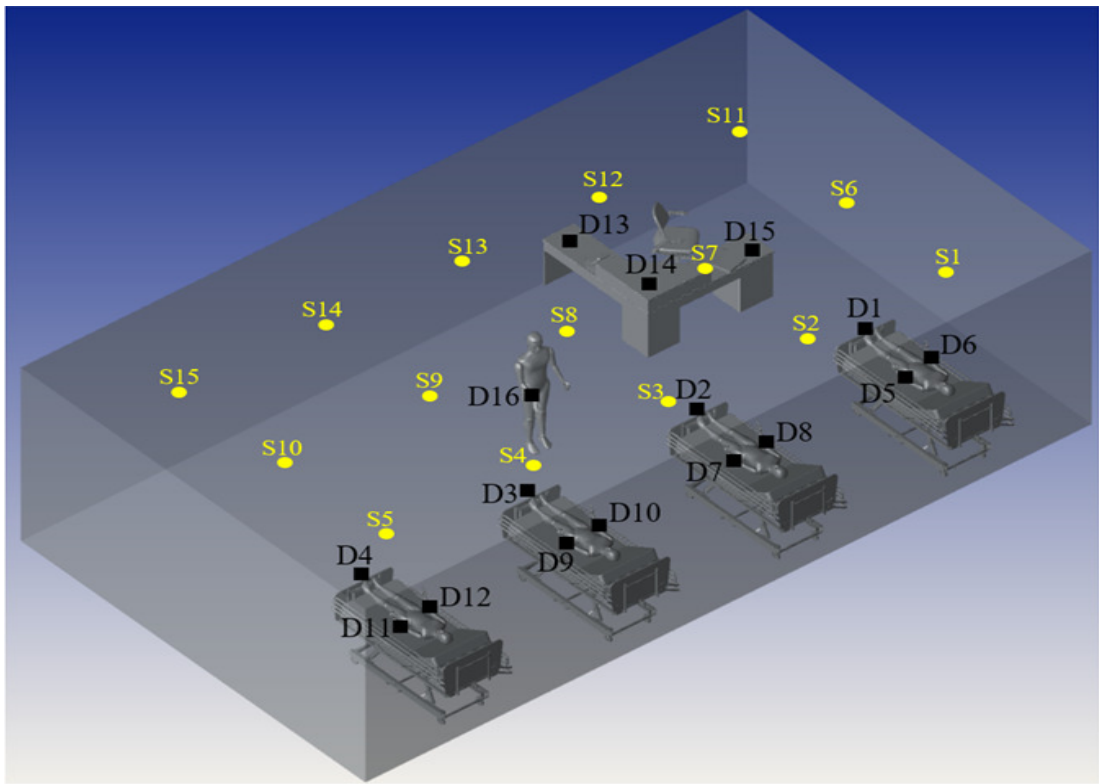
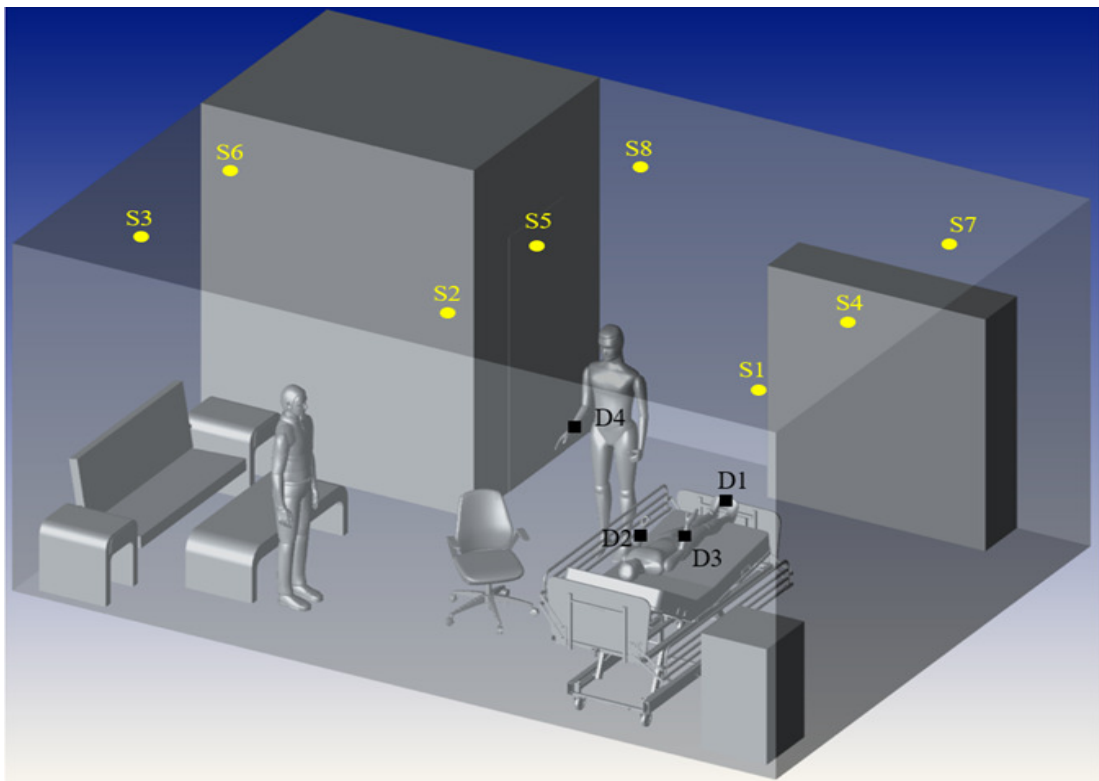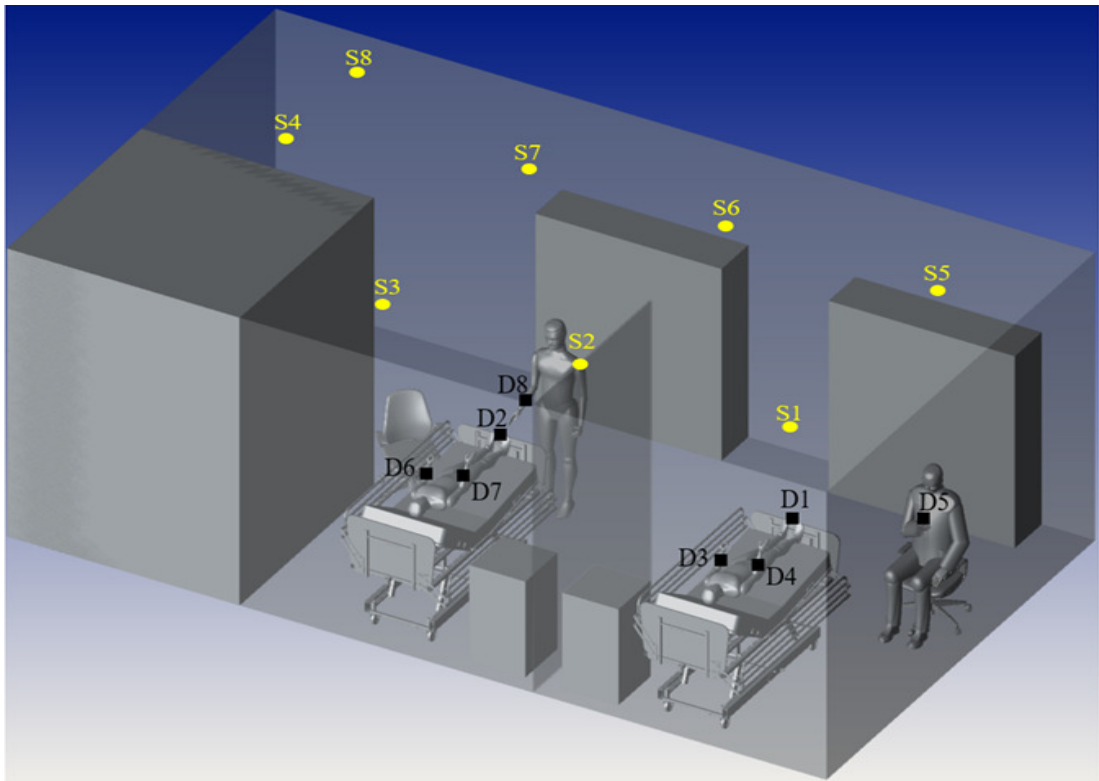Figure 3.7: Hospital room scenarios under consideration. Top: ICU ward. Bottom: Clinic

Figure 3.8: Hospital room scenarios under consideration (continued). Top: Semi-private patient room. Bottom: Family-centered patient room

The sample CIRs for this scenario are shown in Figs. 3.13. It is observed from $h_{S_2D_3}(t)$ that the LoS rays are dominant since the detector D3 on top of the the medical ultrasound machine is located in close proximity to the VLC source. On the other hand, it is observed from $h_{S_5D_2}(t)$ that the diffused rays are significant since detector D2 placed upon the patient's arm collects extensive amount of diffused rays.

3.4.3 Semi-Private Patient Room

In this scenario, a semi-private patient room consisting of two patients lying on their beds, a standing medical staff, and a patient's companion sitting at the bottom side of the corresponding patient's bed is considered. Moreover, a curtain is placed between the drawers next to the patient beds, and wardrobes for each patient are located against the beds (Fig. 3.8). The dimensions of semi-private patient room is 8.8 m × 5 m × 3 m that includes a toilet with dimensions 2.5 m × 2.5 m × 3 m. There are 8 luminaires uniformly located on the ceiling. Due to existence of a toilet room, the room is divided into two sections, with the first section containing the patient's beds and the second one containing the wardrobes. As illustrated in Fig. 3.10, for the first section, the illuminance uniformity, minimum, maximum and average values of illumination are respectively calculated as 0.78, 45.53 lx, 66.69 lx, and 58.21 lx while they are respectively calculated as 0.76, 43.92 lx, 66.04 lx, and 57.97 lx for the second section of the room (Fig. 3.10). It is observed that the illumination requirements for whole room can be satisfied as per requirements in [90, 91]. Eight different locations are also considered for PDs (D1,...,D8). A PD is located on the top side of the foot plate of each patient bed, a pair of PDs is placed on right and left inner arms of each laying patient, a PD is positioned on the wrist of the medical staff, and the last PD is placed on top of the cell phone of patient's companion.

The sample CIRs for this scenario are shown in Figs. 3.14. It is observed from $h_{S_1D_1}(t)$ that the LoS rays are dominant since the detector D1 placed on top of the
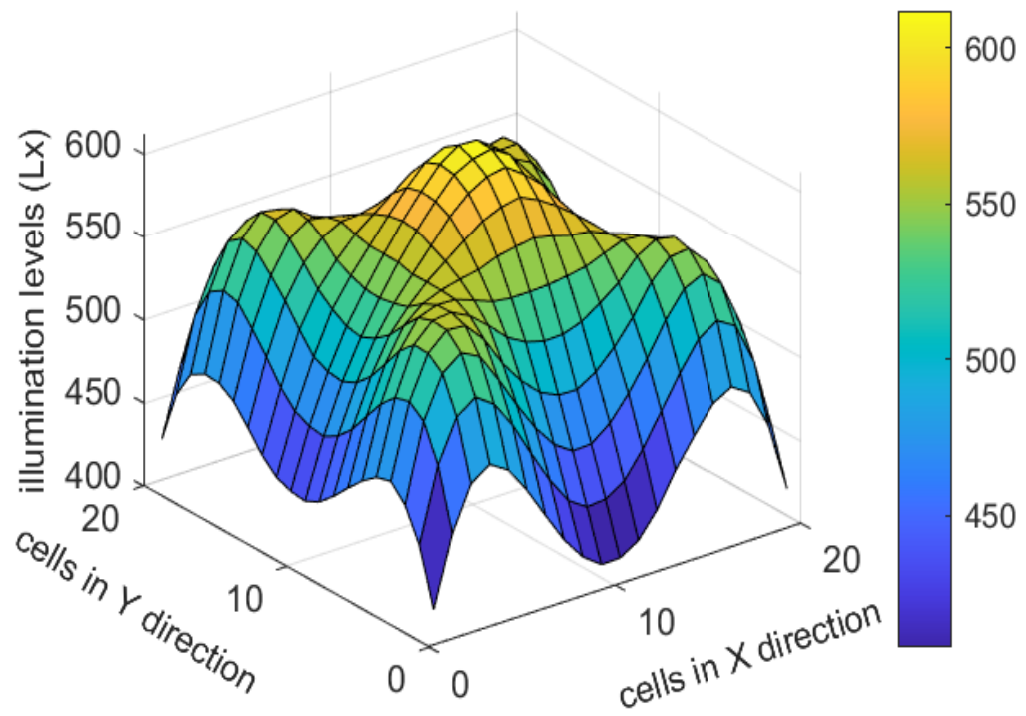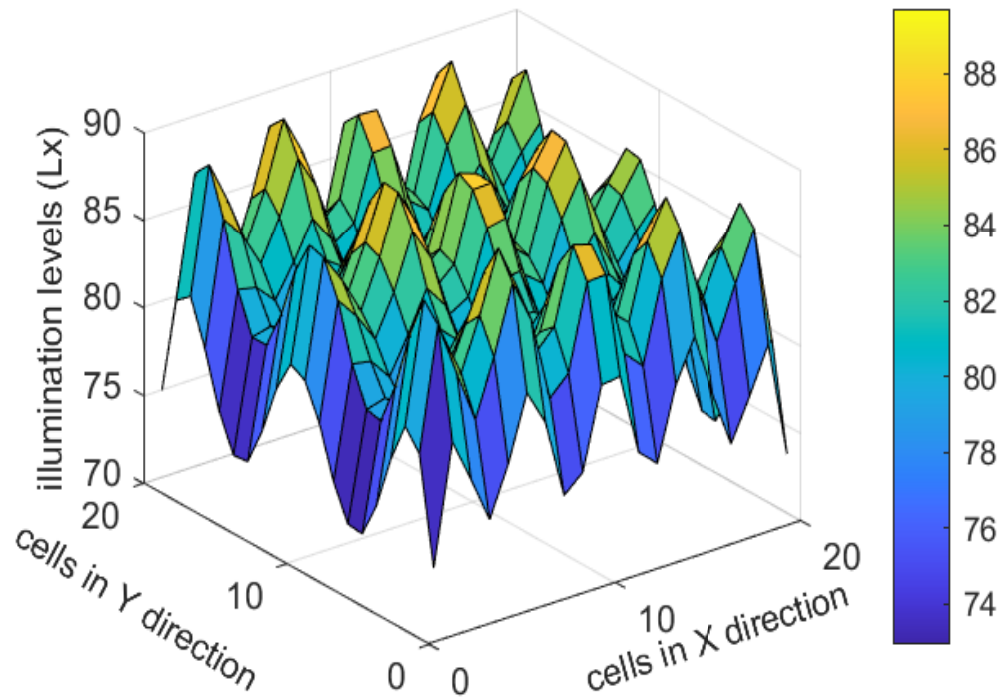
Figure 3.9: Illumination levels of scenarios under consideration. Top: ICU ward.
Bottom: Clinic.
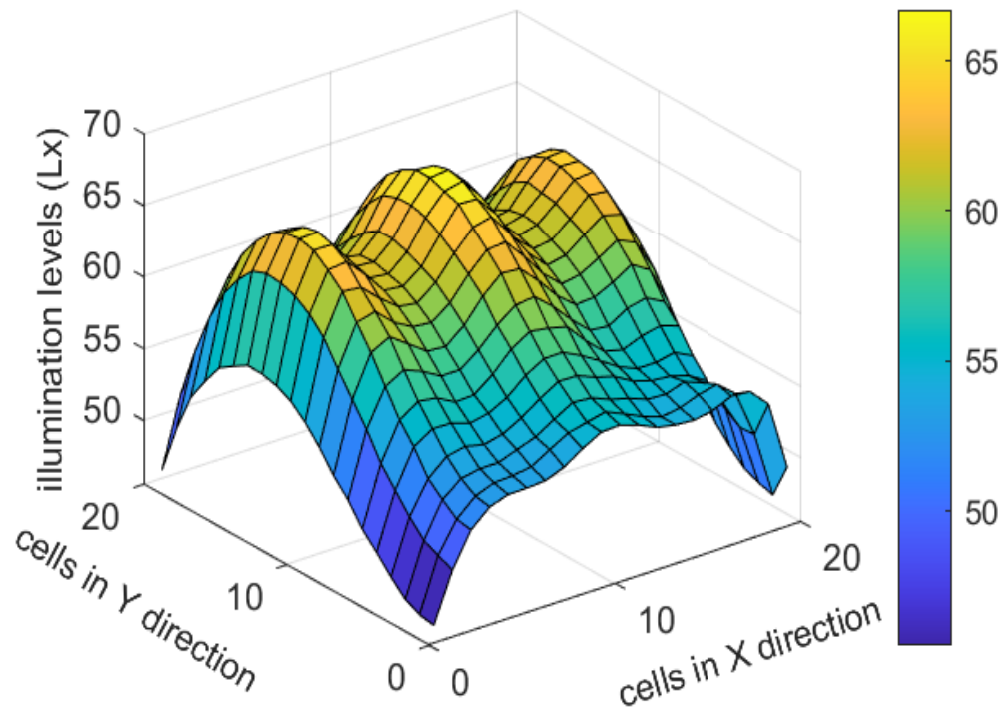
Figure 3.10: Illumination levels of scenarios under consideration. Top: First region of semi-private patient room. Bottom: Second region of semi-private patient room.
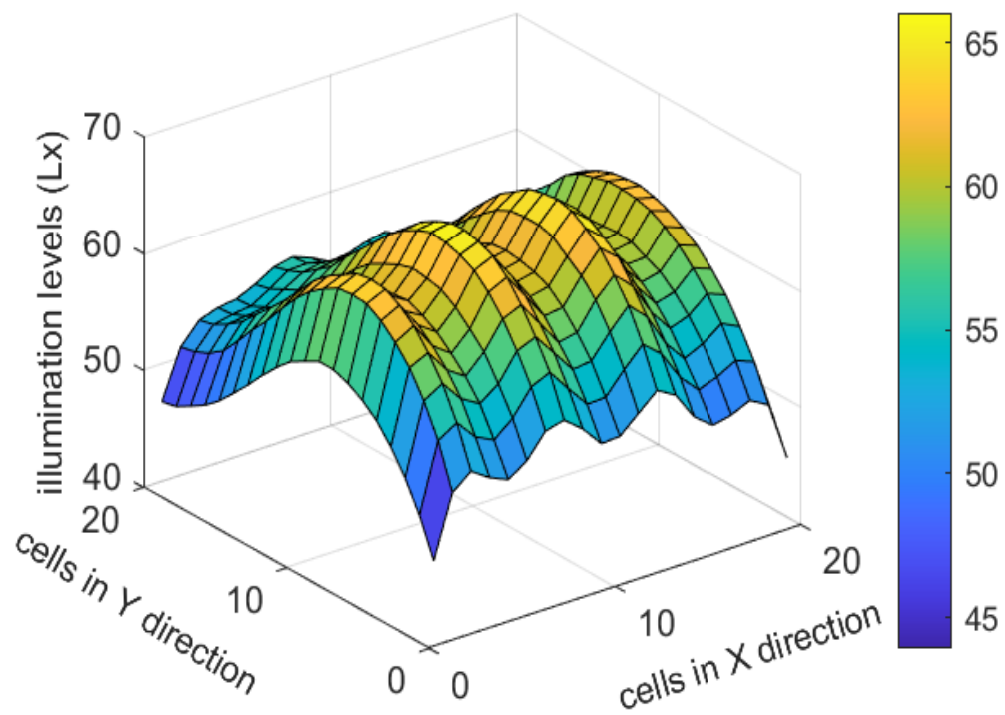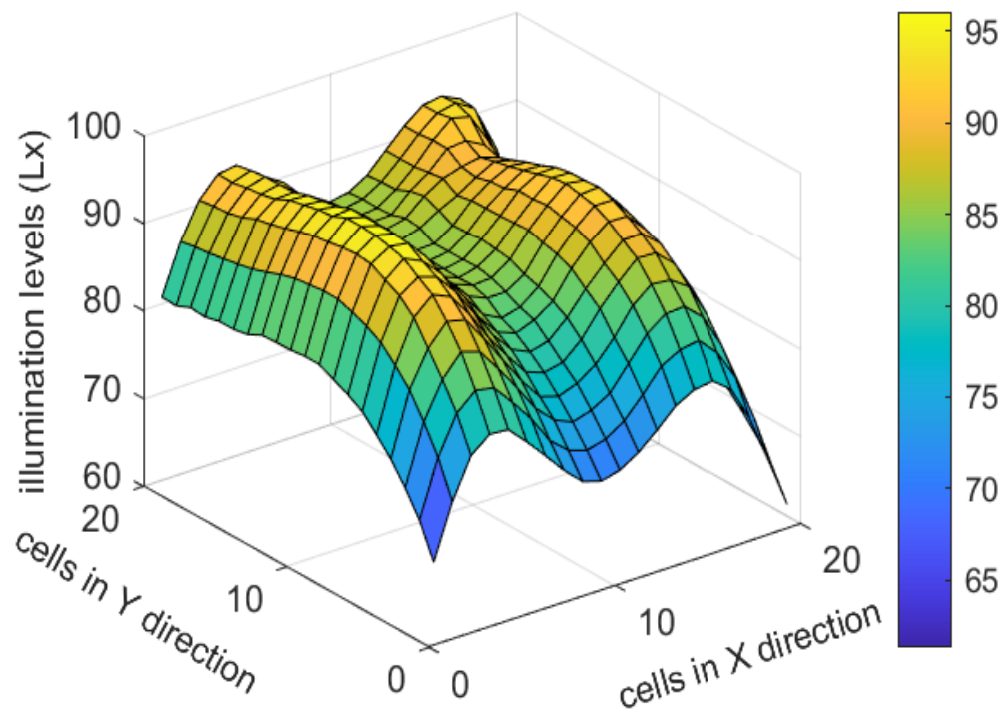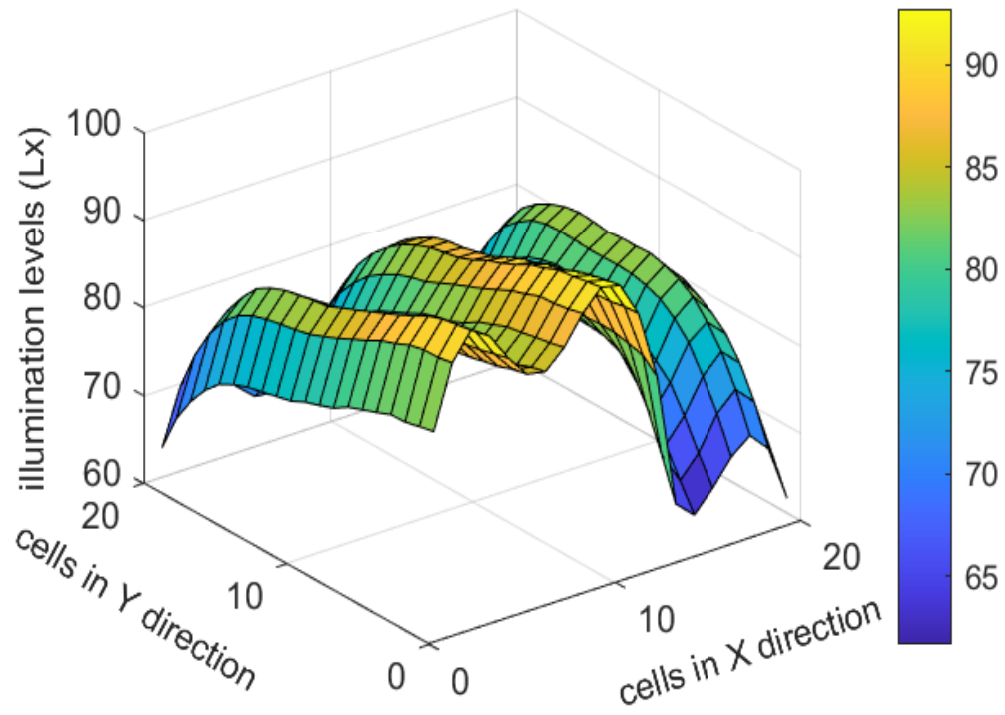
Figure 3.11: Illumination levels of scenarios under consideration. Top: First region of family-centered patient room. Bottom: Second region of family-centered patient room.

patient bed's footboard is located closely to the VLC source. On the other hand, it is observed from $h_{\mathrm{S_8D_6}}(t)$ that diffused rays are dominant since the detector D6 on MBSN node worn by the patient is blocked by the WC walls within the room.

3.4.4 Family-Centered Patient Room

In the last scenario, a family-centered patient room which consists of a single patient laying on the bed, a standing medical staff, and a patient's companion standing in front of the sofa bed and coffee table set is considered. Moreover, a drawer placed next to the patient bed, and a wardrobe is located against the beds (Fig. 3.8). The dimension of semi-private patient room is 7 m $\times$ 5 m $\times$ 3 m including a toilet whose dimension is 2.5 m $\times$ 2 m $\times$ 3 m. There are 8 luminaires uniformly located on the ceiling. Due to existence of a toilet room, we divide the room into two sections, i.e., the first section contains the patient's bed and the second one contains the wardrobe. As illustrated in Fig. 3.11, for the first section of the room, the illuminance uniformity, minimum, maximum and average values of illumination are respectively calculated as 0.77, 61.66 lx, 92.74 lx, and 80.34 lx while they are respectively calculated as 0.71, 61.34 lx, 96.04 lx, and 85.83 lx for the second section of the room (Fig. 3.11). Four different locations are also considered for PDs (D1,...,D4). A PD is located on the top side of the foot plate of each patient bed, a pair of PDs is placed on right and left inner arms of each laying patient, and the last PD is positioned on the wrist of the medical staff.

The sample CIRs for this scenario are shown in Figs. 3.15. It is observed from $h_{\mathrm{S_5D_4}}(t)$ that the LoS rays are dominant since the the nurse wearing on her right hand side a smartwatch upon which a detector D4 is placed stands just under the VLC source. On the other hand, it is observed from $h_{\mathrm{S_7D_2}}(t)$ that the NLoS rays are dominant because the detector D2 upon which is placed the left arm of the patient is oriented towards the opposite direction of the source S7 and hence collects the reflected rays within the room.

Figure 3.12: Sample CIRs for scenarios under consideration. Top to Bottom: CIRs obtained in ICU ward.
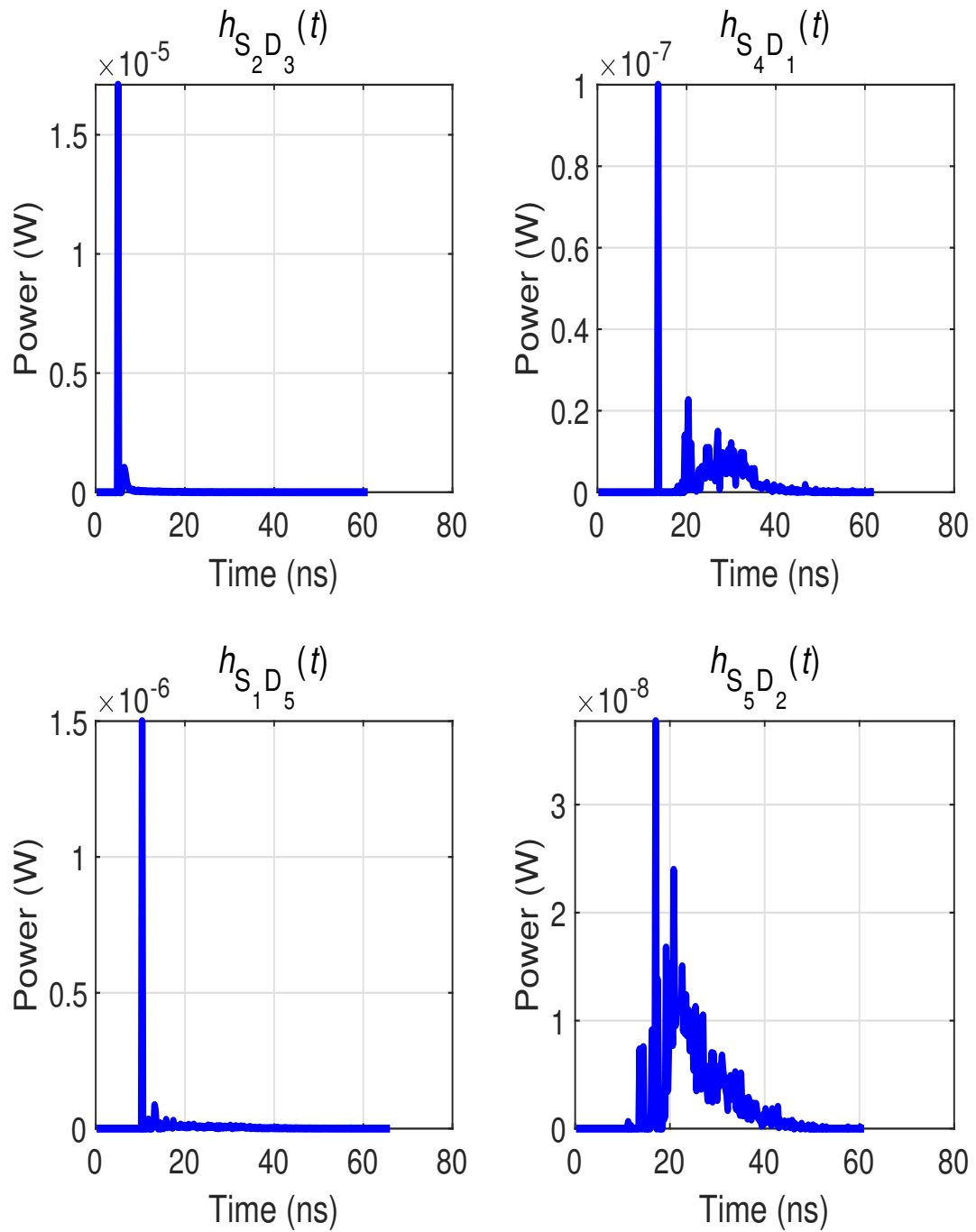
Figure 3.13: Sample CIRs for scenarios under consideration (continued). Top to Bottom: CIRs obtained in clinic.
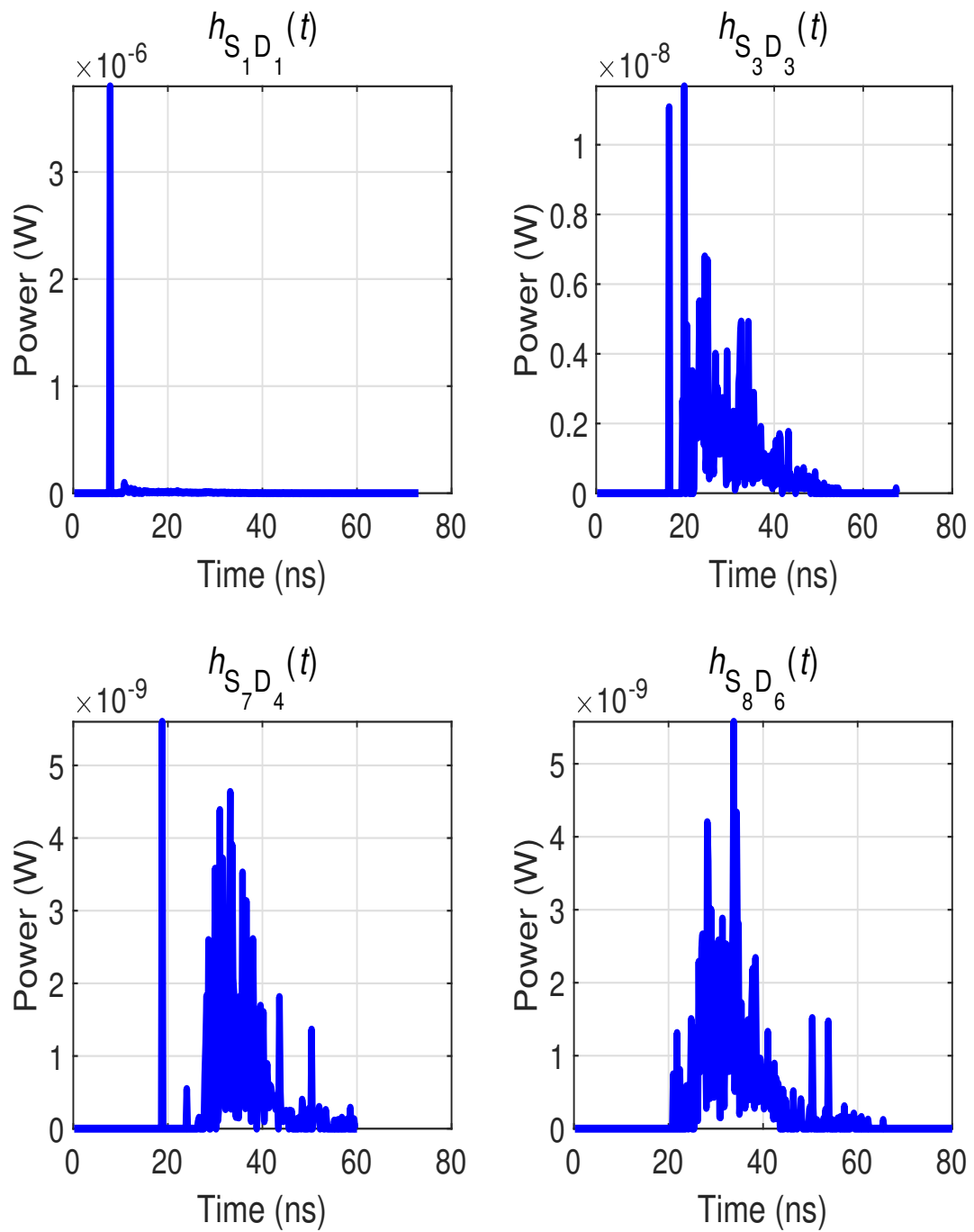
Figure 3.14: Sample CIRs for scenarios under consideration (continued). Top to Bottom: CIRs obtained in semi-private patient room.
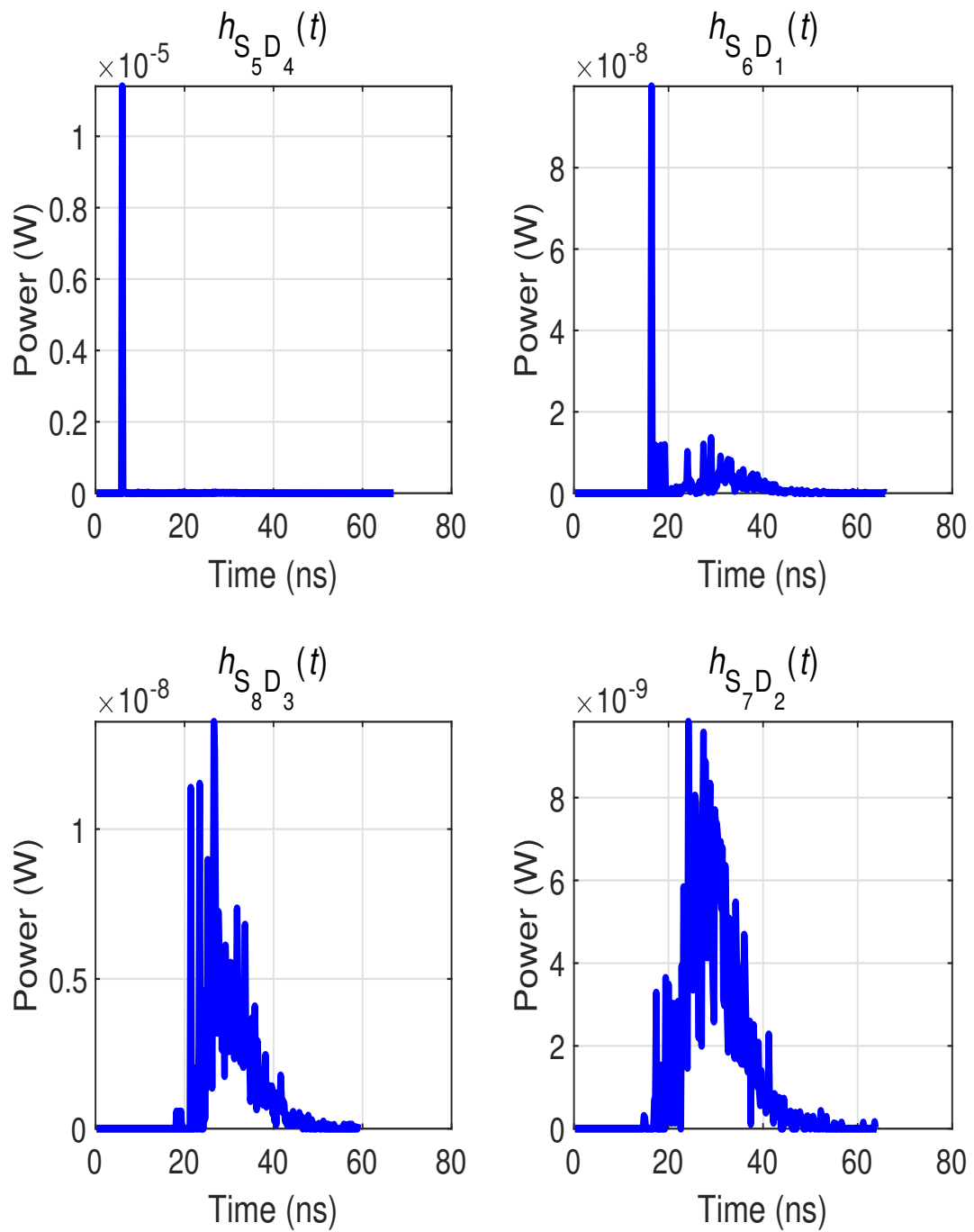
Figure 3.15: Sample CIRs for scenarios under consideration (continued). Top to Bottom: CIRs obtained in family-centered patient room.

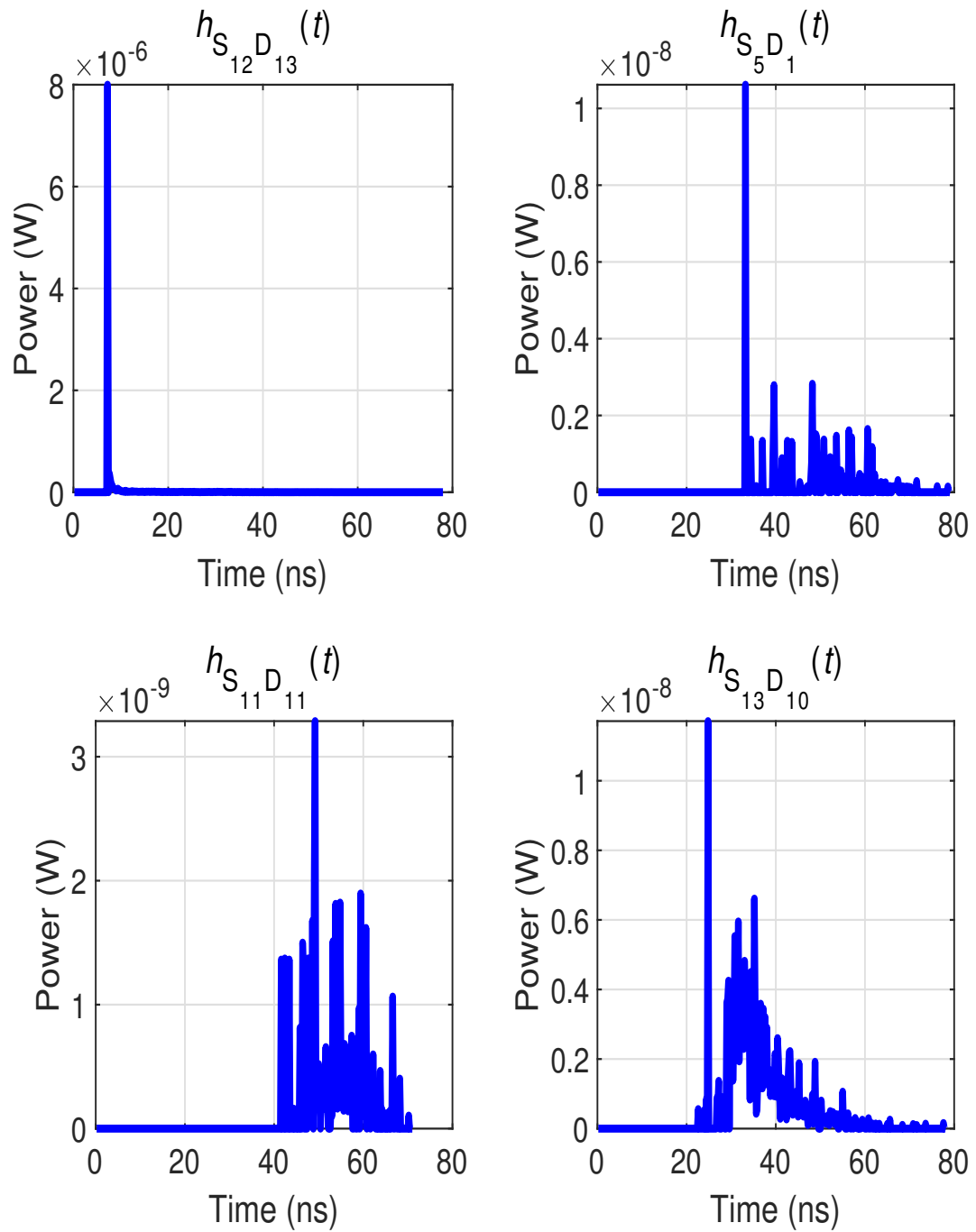It is indeed noteworthy that the frequency selectivity arises mainly due to the multipath reflections (i.e., the NLoS components), however, the deep fade in the frequency response is due to the existence of multiple luminaires due to which multiple LoS components with different delays are received at the photodetector.

The channel characteristics of sample CIRs for reference scenarios under consideration are also summarized in Table 3.7. It is observed from Table 3.7 that the channel DC gains depend on the user location and node location on the patient's body. In fact, the mobility of the MBSNs nodes in an environment causes fluctuations in the received power which necessitates the use of link adaptation to combine the LEDs in a most efficient way and selects modulation order. Furthermore, it is observed from Table 3.7 that the RMS delay spread is in the range 3.51 ns - 10.67 ns. This indicates that for signaling rates lower than 9.37 Msample/sec which can be easily justified for practical needs in MBSNs application, the multipath components are not resolvable and the channel can be modeled as a single-tap (frequency-flat) channel.

Table 3.7: Sample Channel Characteristics of Scenarios Under Consideration

Scenario	Sample CIR	Channel DC Gain H_0	RMS Delay Spread τ_{RMS} (ns)
ICU Ward	$h_{S_{12}D_{13}}(t)$	2.04×10^{-6}	4.98
	$h_{S_5D_1}(t)$	1.09×10^{-8}	10.67
	$h_{S_{11}D_{11}}(t)$	9.09×10^{-9}	6.48
	$h_{S_{13}D_{10}}(t)$	4.45×10^{-8}	7.49
Clinic	$h_{S_2D_3}(t)$	4.76×10^{-6}	3.51
	$h_{S_4D_1}(t)$	1.27×10^{-7}	7.74
	$h_{S_1D_5}(t)$	5.21×10^{-7}	8.11
	$h_{S_5D_2}(t)$	1.40×10^{-7}	6.68
Semi-Private Patient Room	$h_{S_1D_1}(t)$	1.01×10^{-6}	6.38
	$h_{S_3D_3}(t)$	4.26×10^{-8}	7.75
	$h_{S_7D_4}(t)$	2.13×10^{-8}	6.87
	$h_{S_8D_6}(t)$	2.69×10^{-8}	7.29
Family-Centered Patient Room	$h_{S_5D_4}(t)$	2.46×10^{-6}	5.58
	$h_{S_6D_1}(t)$	8.65×10^{-8}	9.00
	$h_{S_8D_3}(t)$	6.65×10^{-8}	5.58
	$h_{S_7D_2}(t)$	8.21×10^{-8}	6.05

In addition to the multipath propagation environment, the effect of LED source should be further taken into account in channel modeling. The frequency response of the LED is assumed as [45]

$$H_{\text{LED}}(f) = \frac{1}{1 + j\, f/f_{cut-off}} \; .$$ (3.9)

The effective channel frequency response (taking into account the LED characteristics and the skin channel) can be then expressed as $h_{\text{eff}}(t) = h_{\text{LED}}(t) \otimes h_{\text{Skin}}(t) \otimes h_{\text{VLC}}(t)$, or $H_{\text{eff}}(f) = H_{\text{LED}}(f)\, H_{\text{Skin}}(f)\, H_{\text{VLC}}(f)$, where $H_{\text{Skin}}(f)$ and $H_{\text{VLC}}(f)$ denote the frequency responses of the skin and VLC channels, respectively.

Chapter 4

Mobile Channel Modelling in Real-Life Based Hospital Scenarios

In Chapter 3, channel modelling and characterization simulation results are presented in case where the light sources and photodetectors are fixed and hence, point-to-point distances between the transmitters and receivers are maintained. However, when VLC-based MBSNs nodes carrying human body is mobile rather than static, channel modeling and characterization turns into a grueling task. Shadowing or complete blockage can emerge as well as can disappear due to the obstructions including the body itself during the travel over a random trajectory in a room. In addition, modelling a realistic human body mobility is crucial for the creation of random trajectories since people do not i) walk with a fixed step length, ii) adhere only to the four cardinal directions, iii) have to initiate a new path at the door side. Therefore, consideration of realistic random trajectories, and wavelength dependency together leads us to model and characterize practical dynamic VLC-based MBSNs channels.

The existing works on mobile IR uplink MBSNs channel models mainly consider random locations rather than random trajectories. In [49], Gaussian distribution is preferred for body positioning whereas the uniform distribution is selected in [54, 55]. However, a random trajectory is taken into account in [58] while modelling the mobility.

The previous works on VLC-based MBSNs consider random locations only. In [60], the positioning of the mobile body is determined based on the uniform distribution.

In Chapter 4, we implement our human mobility model which will be explained in the following section to two real-life based hospital scenarios which are ICU ward and Family-Centered Patient Room (FCPR) so we can analyze the impact of mobility over random trajectories on channel modelling and characterization. Based on the simulation results we obtain, we will explore the spatial distribution and corresponding distribution approximation of the channel DC gain and RMS delay spread.

4.1 Generation of The Random Trajectories

The current studies of mobile channel models on VLC-based MBSNs focus on the randomly selected points within an environment. We propose an algorithm to generate successive random points of which a random trajectory is composed.

The length L and width W of a hospital room are initialized together with an $\mathbf{S}_{2\times2}$ matrix storing the boundaries of the clear area within the room. Both the step length and the direction angle, whose ranges are $(300, 600)$ mm and $(0, 2\pi)$ rad, respectively, are selected uniformly. A mobile user can terminate a random walk somewhere in the room then start a new trajectory thus, the initial point $\mathbf{P}(1, :)$ within a room is generated randomly. Each successive point is determined by the randomly generated steps and is stored in $\mathbf{P}_{10\times2}$. Finally, the algorithm checks whether the points over a random trajectory are located within the clear area boundaries.

We utilize Matlab® to generate the random trajectory based on the random step size and angle, that enable the 3D user mobility.

In simulations, we consider two reference hospital room scenarios with 20 random trajectories for each. Any of these trajectories is constructed by 10 successive

---
Algorithm 1: Random Trajectory Generator

0: Initialize:
L, W, $\mathbf{S}$, $300 \le d \le 600$, $0 \le \theta \le 2\pi$, and $\mathbf{P}$;
0: Coordinates of the starting point, $x_1 \in (0, L)$ & $y_1 \in (0, W)$ are generated randomly. ;
$x_1 =$ random($[0, W], 1$); $y_1 =$ random($[0, L], 1$);
$\mathbf{P}(1, :) = [x_1, y_1]$;
0: Random values for $d \in (300, 600)$ and $\theta \in (0, 2\pi)$ are generated to construct the remaining successive sample points on the trajectory. ;
   for $i=2 \leftarrow 10$ **do**
    $d =$ random($[300, 600], 1$);
    $\theta =$ random($[0, 2\pi], 1$);
    $\mathbf{P}(i, :) = [\mathbf{P}(i-1, 1) + d \cdot cos(\theta), \mathbf{P}(i-1, 2) + d \cdot sin(\theta)]$;
0: The coordinates of 10 points over a trajectory in $\mathbf{P}$ are checked whether an overlap with objects occur or not.;
   for $j=1 \leftarrow 10$ **do**
   if $\mathbf{S}(1, 1) \le \mathbf{P}(j, 1) \le \mathbf{S}(1, 2)$ & $\mathbf{S}(2, 1) \le \mathbf{P}(j, 2) \le \mathbf{S}(2, 2)$ **then**
    print A random trajectory is constructed successfully.
   else
    print An error message.
0: **return** $\mathbf{P}$;
   $=0$

---

random sample points and for illustration purpose we present a sample trajectory for each scenario in Figs. 4.1 and 4.2. In addition, the orientations of the human body as well as the detectors (D1-D3) on MBSNs nodes at the sample points depend on the following point over the trajectory.

4.2 Real-Life Based Hospital Scenarios

We conduct an extensive amount of simulations in ICU ward and FCPR thus, we can only present sample CIRs and sample channel characteristics for a sample point and sample trajectory, respectively.

Channel DC gains and RMS delay spreads, which are the VLC channel characteristics, are determined once CIRs at each sample position over random trajectories
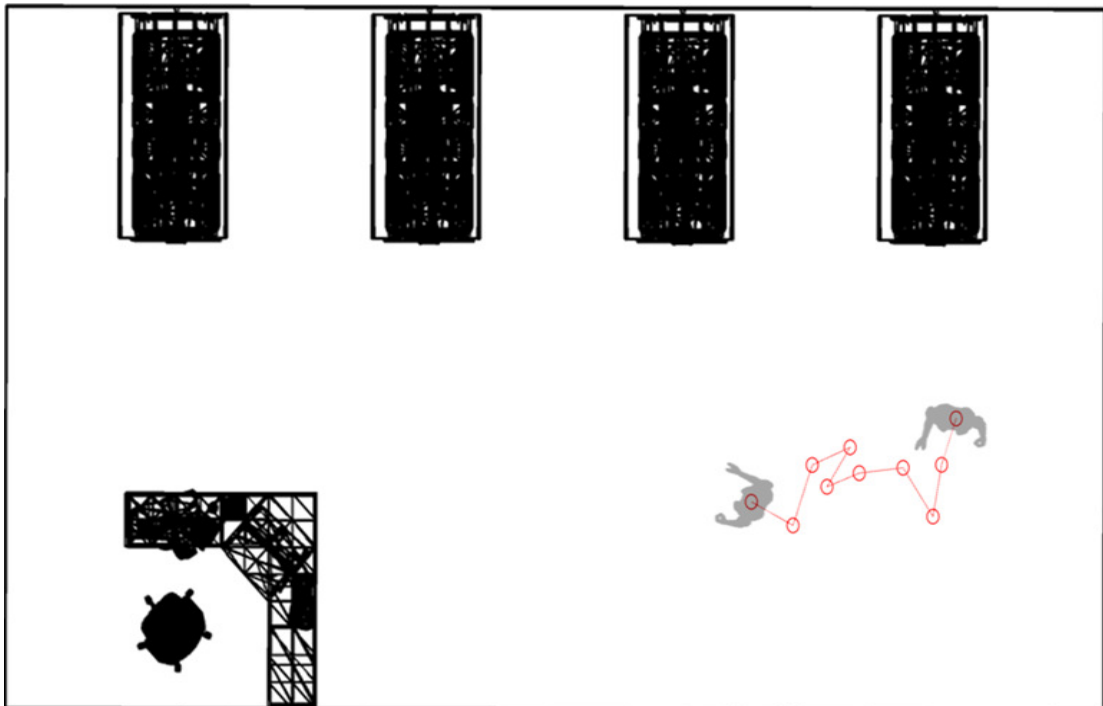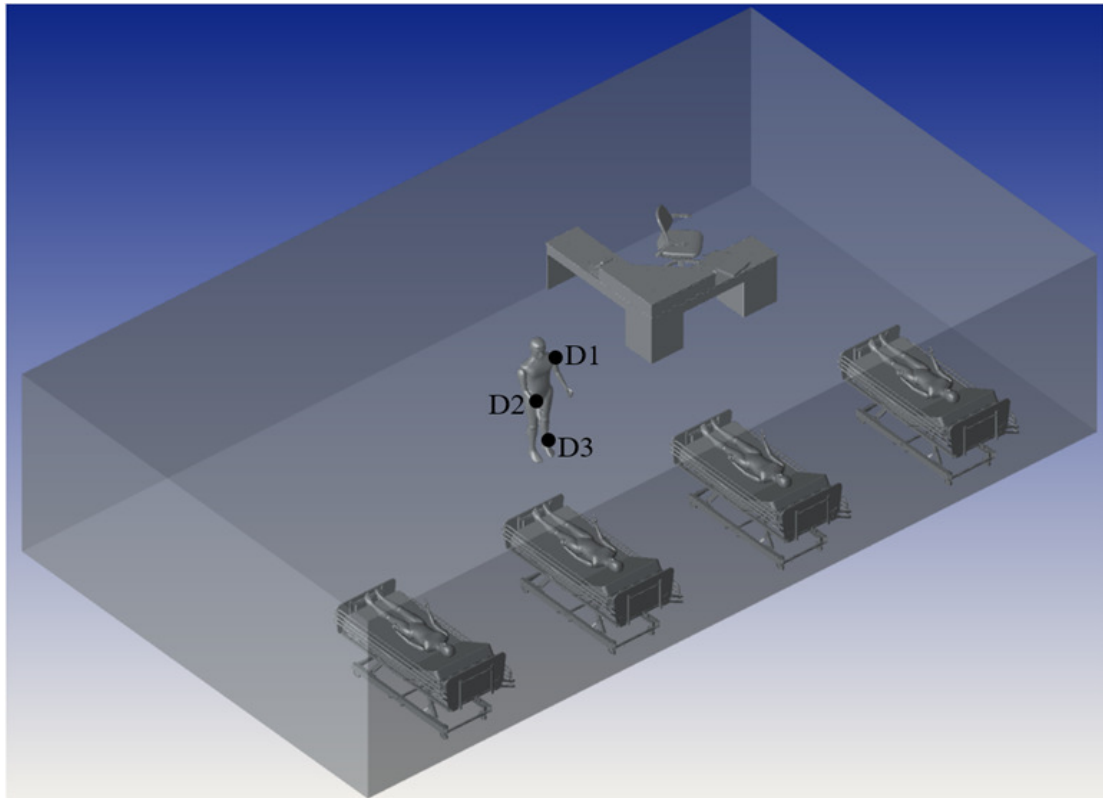
Figure 4.1: ICU scenario. Top: PD Locations. Bottom: A sample trajectory.
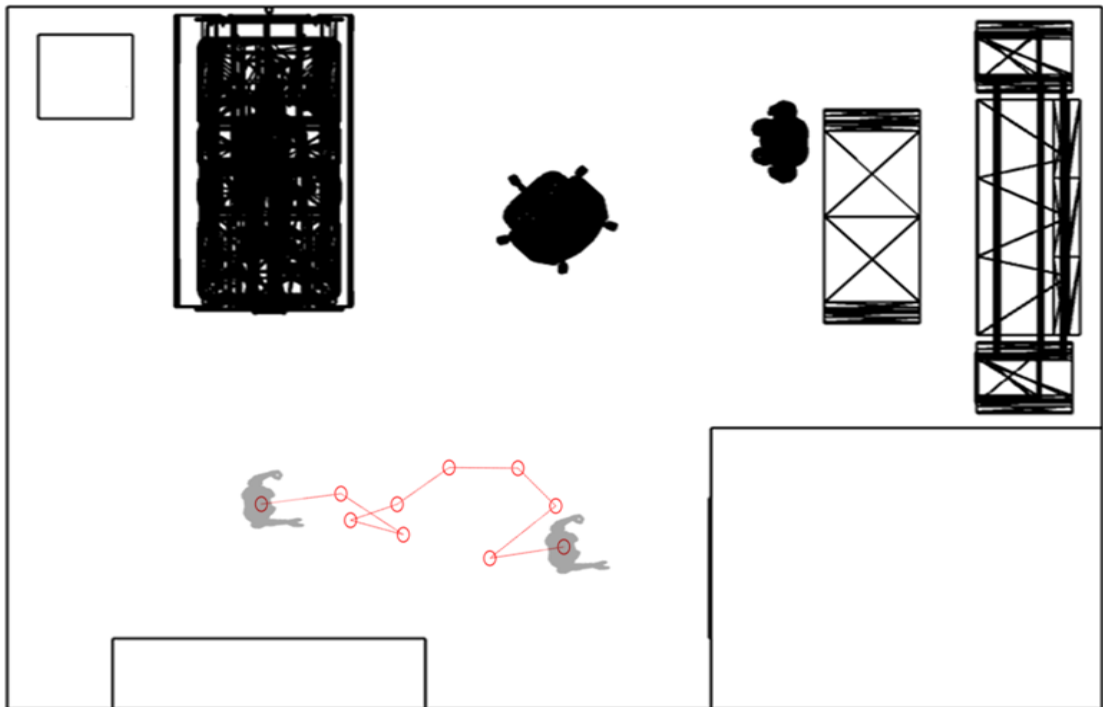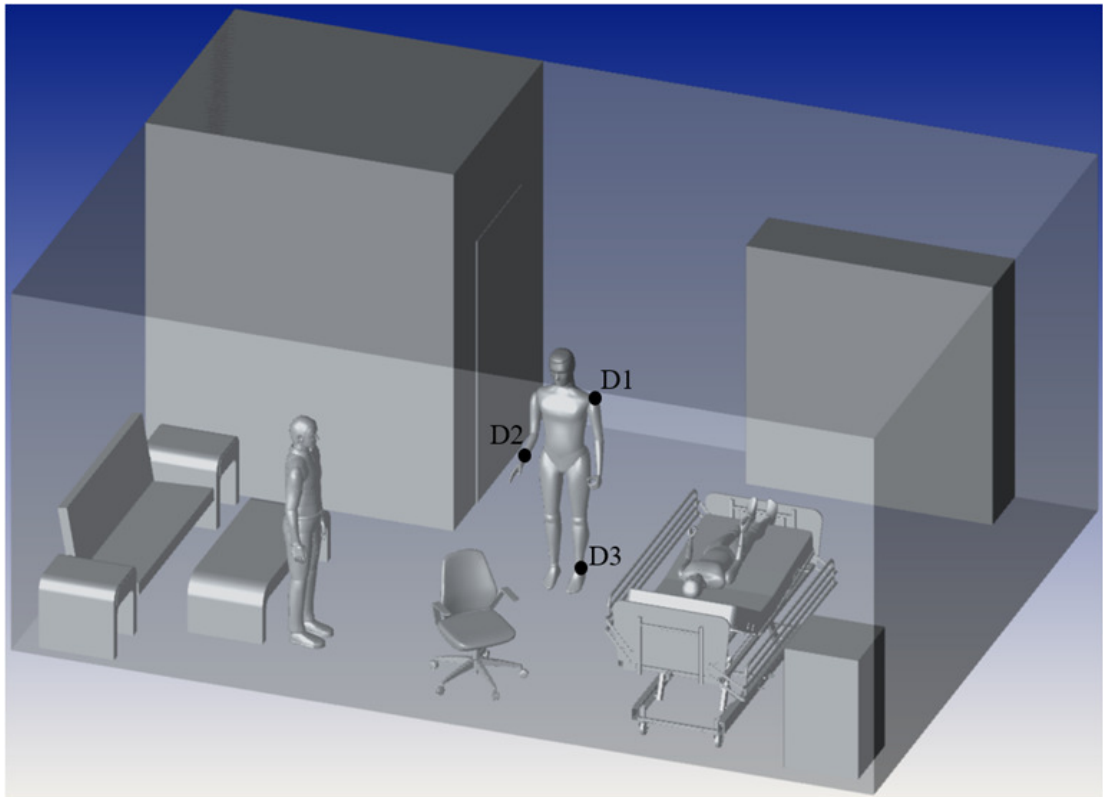
Figure 4.2: Family-centered patient room scenario. Top: PD Locations. Bottom: A sample trajectory.

are obtained. Channel DC gain enables to compute the achievable SNR for a constant source power. On the other hand, RMS delay spread facilitates to figure out the achievable data transmission rate.

4.2.1 ICU Ward

The CIRs associated with D1–D3 at a sample point over a trajectory in ICU ward are presented in Figs. 4.3. It is observed from $h_{\mathrm{P_8D_1}}(t)$ and $h_{\mathrm{P_8D_2}}(t)$ that the LoS rays are dominant since the detector D1 placed on the shoulder and detector D2 located on the wrist are able to collect many LoS rays due to their higher location and upward orientation. On the other hand, $h_{\mathrm{P_8D_3}}(t)$ shows the dominance of diffused rays when the received power and the Time-of-Arrival (TOA) of the first multi-path component are compared with those for D1 and D2.

Table 4.1: Channel DC Gains of Sample Trajectory Points in ICU Ward

Trajectory No: 14	Channel DC Gain H_0		
Point No.	**D1**	**D2**	**D3**
P1	2.20×10^{-7}	2.06×10^{-7}	8.99×10^{-8}
P2	1.78×10^{-7}	1.62×10^{-7}	1.12×10^{-7}
P3	2.21×10^{-7}	4.02×10^{-7}	9.43×10^{-8}
P4	2.35×10^{-7}	2.55×10^{-7}	1.52×10^{-7}
P5	2.06×10^{-7}	1.76×10^{-7}	1.73×10^{-7}
P6	2.49×10^{-7}	2.05×10^{-7}	1.10×10^{-7}
P7	1.94×10^{-7}	2.35×10^{-7}	1.45×10^{-7}
P8	2.05×10^{-7}	2.40×10^{-7}	1.19×10^{-7}
P9	3.28×10^{-7}	3.02×10^{-7}	9.11×10^{-8}
P10	2.50×10^{-7}	1.88×10^{-7}	1.42×10^{-7}

The channel DC gains and RMS delay spreads associated with D1–D3 for a sample trajectory in ICU ward are presented in Table 4.1 and Table 4.2, respectively. Moreover, it is observed from Table 4.2 that the RMS delay spread is in the range 9.02 ns - 13.26 ns. This indicates that for signaling rates lower than 7.54 Msample/sec which can be easily justified for practical needs in MBSNs application, the multipath components are not resolvable and the channel can be modeled as a single-tap (frequency-flat) channel.
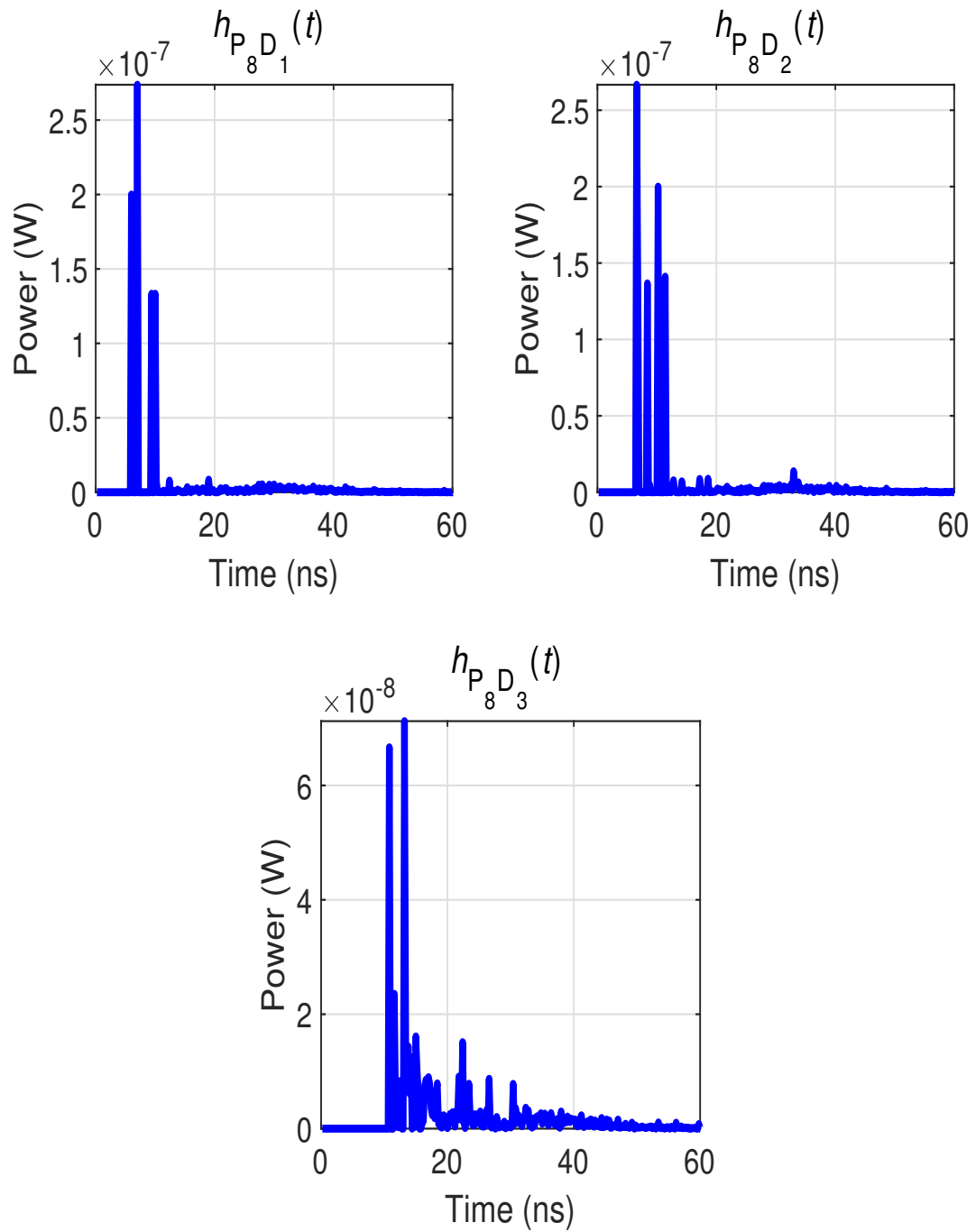
Figure 4.3: Sample CIRs for PDs placed on three different parts of the body located in ICU ward. Top Left: Shoulder (D1). Top Right: Wrist (D2). Bottom: Ankle (D3).

Furthermore, we demonstrate the spatial distribution of channel DC gains and RMS delay spreads associated with D1, D2 and D3 which are placed on the

Table 4.2: RMS Delay Spreads of Sample Trajectory Points in ICU Ward

Trajectory No: 14	RMS Delay Spread τ_{RMS}		
Point No.	**D1** (ns)	**D2** (ns)	**D3** (ns)
P1	11.78	11.80	10.81
P2	12.02	12.60	10.57
P3	11.53	9.02	11.60
P4	10.95	11.12	10.86
P5	11.61	12.98	10.14
P6	11.82	11.25	11.91
P7	11.97	11.51	10.92
P8	11.39	11.50	11.52
P9	10.65	11.07	13.26
P10	11.26	13.06	10.87

mobile human body walking over different random trajectories[1], in Figs. 4.4–4.6 and 4.7–4.9, respectively.

Channel DC gain values in Figs. 4.4 and 4.5 increase as the body comes closer to the luminaries however, it displays a flatten surface as shown in 4.6 because D3 can collect only NLoS rays. The range of the channel DC gains for D1, D2, and D3 among 200 different positions are $0.69 - 4.89 \times 10^{-7}$, $1.00 - 4.02 \times 10^{-7}$, $0.66 - 2.51 \times 10^{-7}$, respectively.

The histograms of channel DC gains associated with photodetectors D1, D2, and D3, are presented together with the corresponding spatial distribution of H_0 in Figs. 4.4–4.6. Each histogram shows the number of times that channel DC gains exist within specified intervals. By curve fitting, we discover that Generalized Extreme Value (GEV) distribution approximates good on the histogram [92]. The distribution is given as

$$f\left(H_0\right) = \left(\frac{1}{\sigma}\right) \exp\left(-\left(1 + \xi\frac{(H_0 - \mu)}{\sigma}\right)^{-\frac{1}{\xi}}\right) \times \left(1 + \xi\frac{(H_0 - \mu)}{\sigma}\right)^{-1-\frac{1}{\xi}} \quad (4.1)$$

---

[1]Cell size of 0.5 m × 0.5 m is applied to the reference scenarios under consideration [47]. Based on the selected cell size and floor dimensions of the reference scenarios, different cell numbers are seen along X and Y axes in Figs. 4.4–4.9 and 4.11–4.16

where ξ, σ, and μ denote shape, scale, and location parameters of the distribution, respectively.

The parameters of the GEV distribution for channel DC gains associated with PDs in ICU ward are presented in Table 4.3.

Table 4.3: Generalized Extreme Value Distribution Parameters

	ξ	σ	μ
D1	-0.126	7.34×10^{-8}	1.83×10^{-7}
D2	-0.160	5.41×10^{-8}	2.01×10^{-7}
D3	-0.062	2.91×10^{-8}	1.13×10^{-7}

On the other hand, we present the spatial distribution of RMS delay spread associated with D1, D2 and D3 which are placed on the mobile human body walking over different random trajectories in Figs. 4.7–4.9. The range of RMS delay spread values for D1, D2, and D3 are $9.06 - 14.22$ ns, $9.02 - 14.11$ ns, and $8.94 - 14.09$ ns, respectively. Therefore, a flat fading channel can be modeled in ICU ward if a data rate lower than 7.03 Mbit/s, that is sufficient for MBSNs applications [7], is selected.

The histograms of RMS delay spreads associated with photodetectors D1, D2, and D3, are presented together with the corresponding spatial distribution of τ_{RMS} in Figs. 4.7–4.9. Each histogram shows the number of times that RMS delay spread exist within specified intervals. By curve fitting, we discover that log-normal distribution approximates good on the histogram [93]. The distribution is expressed as

$$f\left(\tau_{\mathrm{RMS}}\right) = \frac{1}{\tau_{\mathrm{RMS}}\sigma\sqrt{2\pi}} \exp\left(-\frac{\left(\ln\left(\tau_{\mathrm{RMS}}\right) - \mu\right)^2}{2\sigma^2}\right) \tag{4.2}$$

where μ and σ denote location and scale parameters of the distribution, respectively. Since μ denotes the most probable channel DC gain value in the PDFs, we can infer that channel DC gain associated with D1 and D2 are similar besides they are larger than that of D3, which was placed on the ankle. This outcome is consistent with the histograms we present.
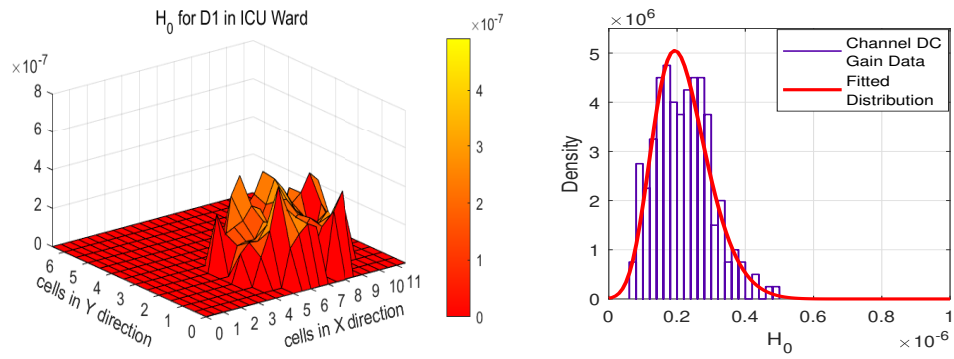
Figure 4.4: Spatial distribution and histogram of channel DC gains associated with D1. Top: Spatial distribution of H_0 for D1. Bottom: Generalized extreme value approximation to H_0 histogram of D1.
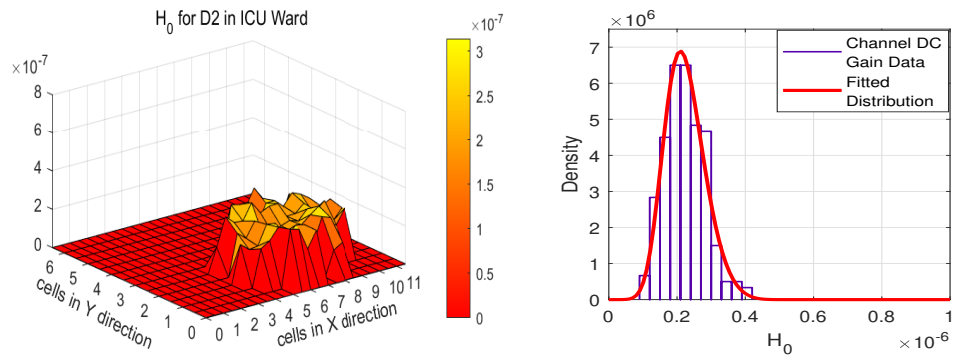
Figure 4.5: Spatial distribution and histogram of channel DC gains associated with D2. Top: Spatial distribution of H_0 for D2. Bottom: Generalized extreme value approximation to H_0 histogram of D2.
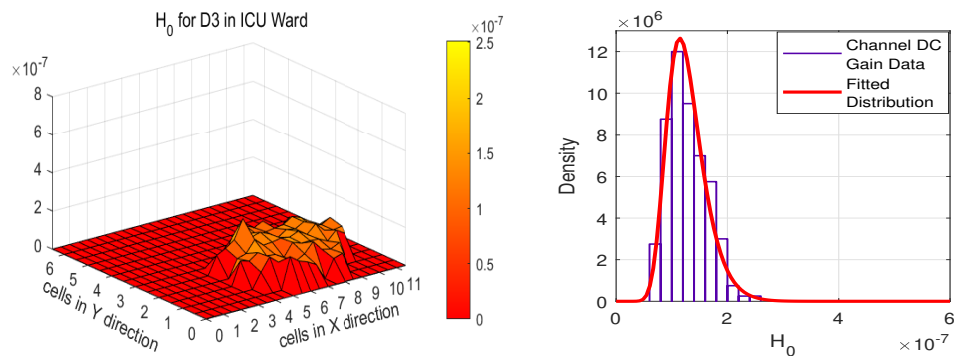
Figure 4.6: Spatial distribution and histogram of channel DC gains associated with D3. Top: Spatial distribution of H_0 for D3. Bottom: Generalized extreme value approximation to H_0 histogram of D3.
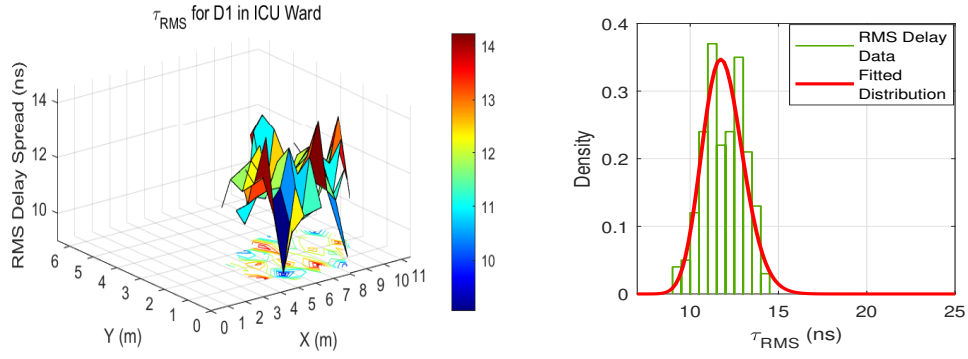
Figure 4.7: Spatial distribution and histogram of RMS delay spreads associated with D1. Top: Spatial distribution of τ_{RMS} for D1. Bottom: Log-normal distribution approximation to τ_{RMS} histogram of D1.
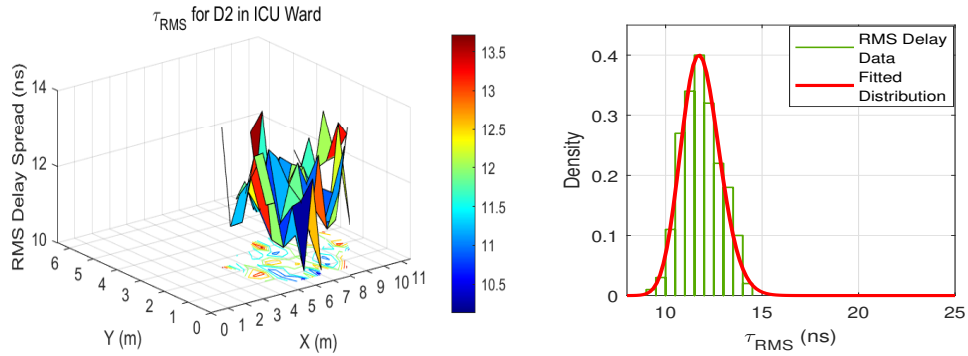
Figure 4.8: Spatial distribution and histogram of RMS delay spreads associated with D2. Top: Spatial distribution of τ_{RMS} for D1. Bottom: Log-normal distribution approximation to τ_{RMS} histogram of D2.
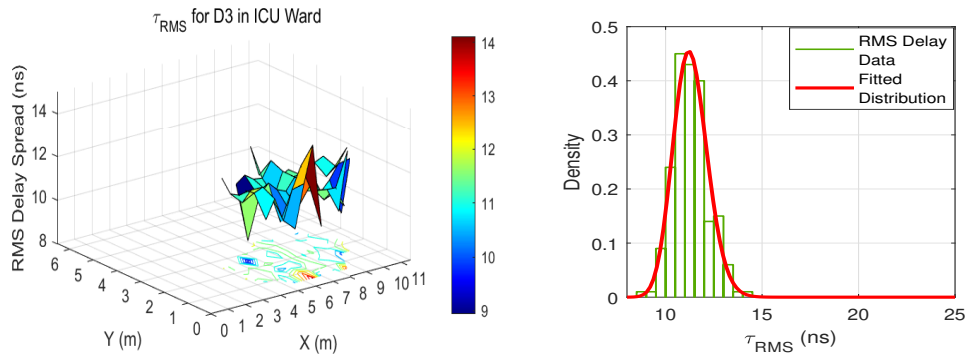
Figure 4.9: Spatial distribution and histogram of RMS delay spreads associated with D3. Left: Spatial distribution of τ_{RMS} for D3. Right: Log-normal distribution approximation to τ_{RMS} histogram of D3.

The parameters of log-normal distribution for RMS delay spreads associated with PDs in ICU ward are presented in Table 4.4.

Table 4.4: Log-Normal Distribution Parameters

	μ	σ
D1	2.472	9.75×10^{-2}
D2	2.469	8.47×10^{-2}
D3	2.422	7.80×10^{-2}

Since μ denotes the most probable RMS delay value in the PDFs, we can infer that RMS values associated with D1–D3 are quite similar. This outcome is consistent with the histograms we present.

4.2.2 Family-Centered Patient Room

The CIRs associated with D1–D3 at a sample point over a trajectory in family-centered patient room are presented in Figs. 4.10. It is observed from $h_{P_6 D_1}(t)$ and $h_{P_6 D_2}(t)$ that LoS rays collected by the PDs placed upon the shoulder and wrist are dominant whereas diffused rays are significant in $h_{P_6 D_3}(t)$ that is due to placement of D3 on the ankle and heading towards the side walls of then room.

The channel DC gains and RMS delay spreads associated with D1–D3 for a sample trajectory in family-centered patient room are presented in Table 4.3 and Table 4.4, respectively. Moreover, it is observed from Table 4.4 that the RMS delay spread is in the range 7.04 ns - 10.15 ns. This indicates that for signaling rates lower than 9.85 Msample/sec which can be easily justified for practical needs in MBSNs application, the multipath components are not resolvable and the channel can be modeled as a single-tap (frequency-flat) channel.

Furthermore, we demonstrate the spatial distribution of channel DC gains and RMS delay spreads associated with D1, D2 and D3 which are placed on the mobile human body walking over different random trajectories, in Figs. 4.11–4.13 and 4.14–4.16, respectively.
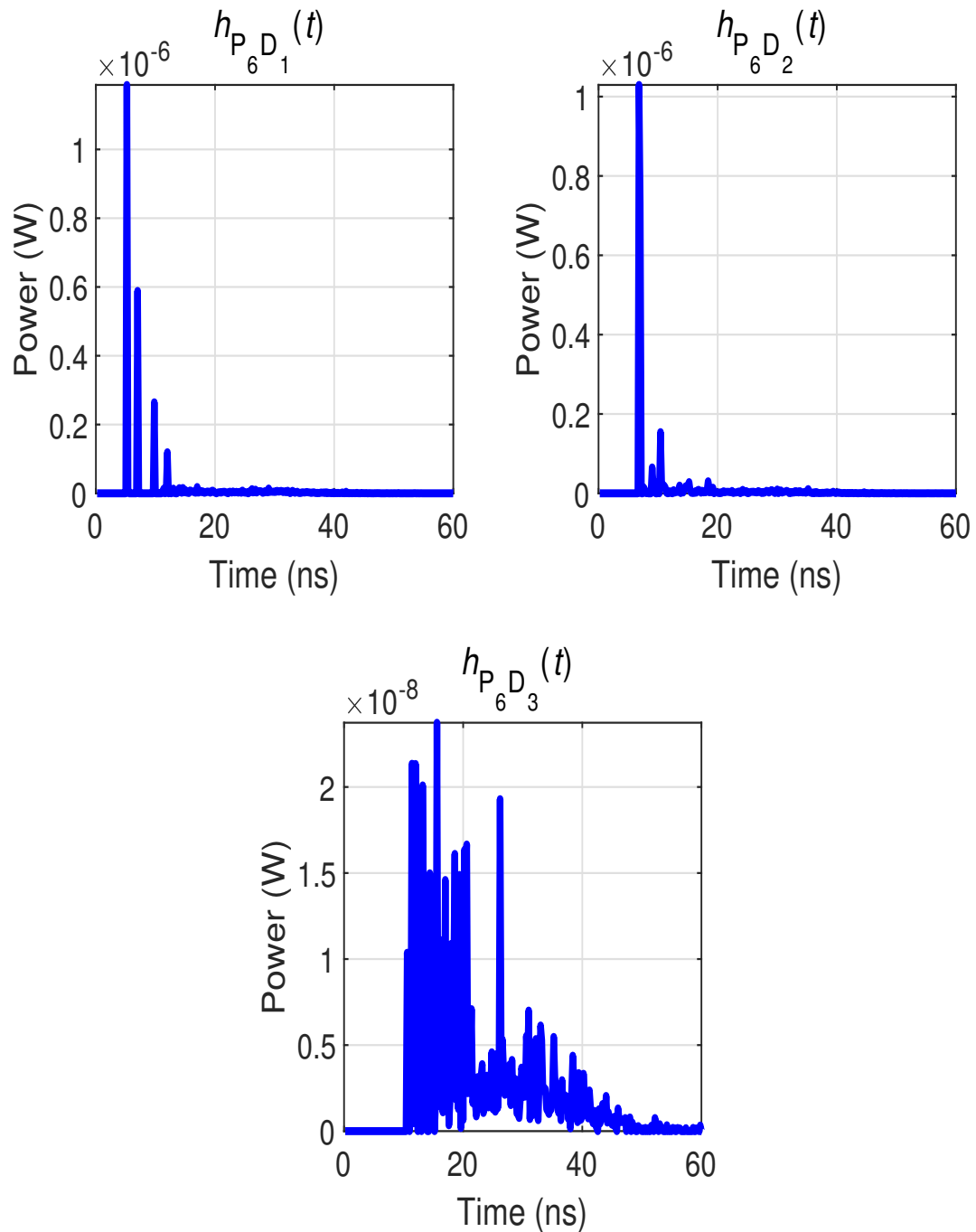
Figure 4.10: Sample CIRs for PDs placed on three different parts of the body located in family type patient room. Top Left: Shoulder (D1). Top Right: Wrist (D2). Bottom: Ankle (D3).

Channel DC gain values in Figs. 4.11 and 4.12 increase as the body comes closer to the luminaries however, it displays a flatten surface as shown in 4.13 because D3 can collect only NLoS rays. The range of the channel DC gains for D1, D2,

Table 4.5: Channel DC Gains of Sample Trajectory Points in FCPR

Trajectory No: 3	Channel DC Gain H_0		
Point No.	**D1**	**D2**	**D3**
P1	4.13×10^{-7}	4.45×10^{-7}	3.28×10^{-7}
P2	5.37×10^{-7}	3.53×10^{-7}	1.78×10^{-7}
P3	4.52×10^{-7}	3.36×10^{-7}	1.44×10^{-7}
P4	3.90×10^{-7}	5.19×10^{-7}	2.47×10^{-7}
P5	4.34×10^{-7}	5.54×10^{-7}	1.72×10^{-7}
P6	5.55×10^{-7}	5.49×10^{-7}	1.35×10^{-7}
P7	5.76×10^{-7}	3.87×10^{-7}	1.91×10^{-7}
P8	5.44×10^{-7}	5.12×10^{-7}	1.84×10^{-7}
P9	5.79×10^{-7}	5.88×10^{-7}	2.83×10^{-7}
P10	3.03×10^{-7}	5.37×10^{-7}	2.80×10^{-7}

Table 4.6: RMS Delay Spreads of Sample Trajectory Points in FCPR

Trajectory No: 3	RMS Delay Spread τ_{RMS}		
Point No.	**D1** (ns)	**D2** (ns)	**D3** (ns)
P1	9.16	8.53	7.88
P2	8.49	8.97	7.13
P3	8.51	9.68	7.66
P4	9.39	8.42	9.50
P5	9.30	8.78	7.87
P6	8.72	8.18	9.71
P7	8.35	8.97	7.14
P8	8.23	8.41	7.04
P9	8.43	7.51	9.04
P10	10.15	7.80	9.51

and D3 among 200 different positions are $2.42 - 7.47 \times 10^{-7}$, $3.08 - 6.97 \times 10^{-7}$, $0.99 - 3.97 \times 10^{-7}$, respectively.

The histograms of channel DC gains associated with photodetectors D1, D2, and D3, are presented together with the corresponding spatial distribution of H_0 in Figs. 4.11–4.13. By curve fitting, we discover that generalized extreme value distribution approximates well on the histograms.

The parameters of the GEV distribution for channel DC gains associated with PDs in family-centered patient room are presented in Table 4.7. Since μ denotes

the most probable channel DC gain value in the PDFs, we can infer that channel DC gain associated with D1 and D2 are similar but they are significantly higher than that of D3 and this result is expected.

Table 4.7: Generalized Extreme Value Distribution Parameters

	ξ	σ	μ
D1	-0.226	8.48×10^{-8}	4.68×10^{-7}
D2	-0.244	7.91×10^{-8}	4.51×10^{-7}
D3	-0.123	4.70×10^{-8}	1.84×10^{-7}

On the other hand, we present the spatial distribution of RMS delay spread associated with D1, D2 and D3 which are placed on the mobile human body walking over different random trajectories in Figs. 4.14–4.16. The range of RMS delay spread values for D1, D2, and D3 are $6.96 - 10.61$ ns, $7.03 - 10.17$ ns, and $6.21 - 10.04$ ns, respectively. Therefore, a flat fading channel can be modeled in ICU ward if a data rate lower than 9.43 Mbit/s, that is sufficient for MBSNs applications [7], is selected.

The histograms of RMS delay spreads associated with photodetectors D1, D2, and D3, are presented together with the corresponding spatial distribution of τ_{RMS} in Figs. 4.14–4.16. By curve fitting, we discover that log-normal distribution approximates well on the histogram.

Table 4.8: Log-Normal Distribution Parameters

	μ	σ
D1	2.155	6.59×10^{-2}
D2	2.146	7.47×10^{-2}
D3	2.070	9.67×10^{-2}

The parameters of log-normal distribution for RMS delay spreads associated with PDs in family-centered patient room are presented in Table 4.8. Since μ denotes the most probable RMS delay value in the PDFs, we can infer that RMS values associated with D1–D3 are quite similar which is expected. The main reason of the parameter value discrepancies between these two scenarios is that the volume of ICU ward is slightly larger than that of family-centered patient room.
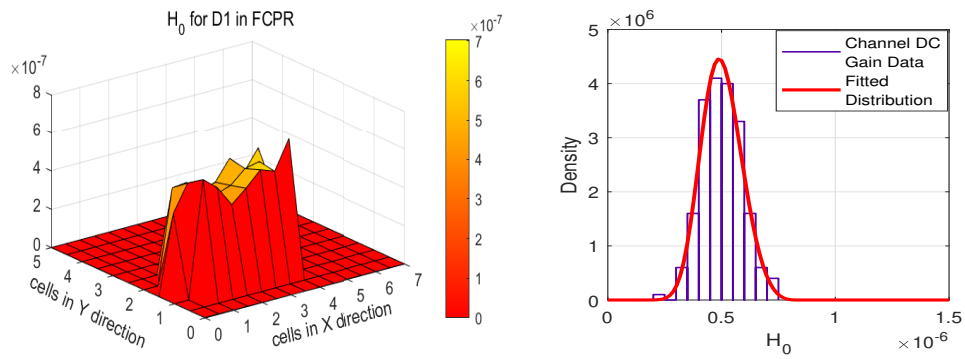
Figure 4.11: Spatial distribution and histogram of channel DC gains associated with D1. Left: Spatial distribution of H_0 for D1. Right: Generalized extreme value approximation to H_0 histogram of D1.
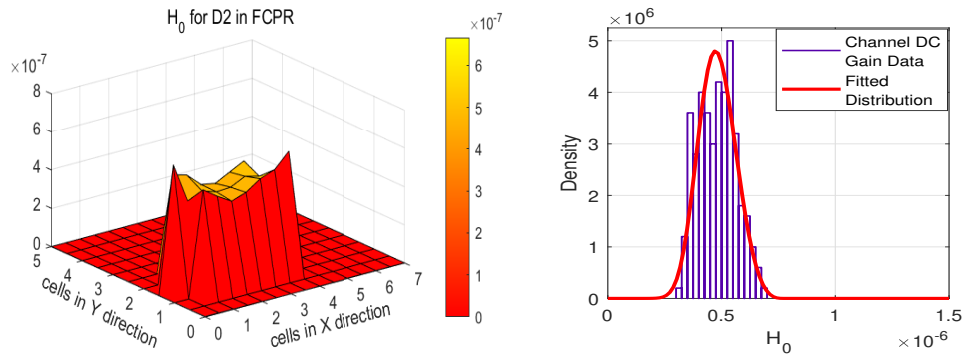
Figure 4.12: Spatial distribution and histogram of channel DC gains associated with D2. Left: Spatial distribution of H_0 for D2. Right: Generalized extreme value approximation to H_0 histogram of D2.
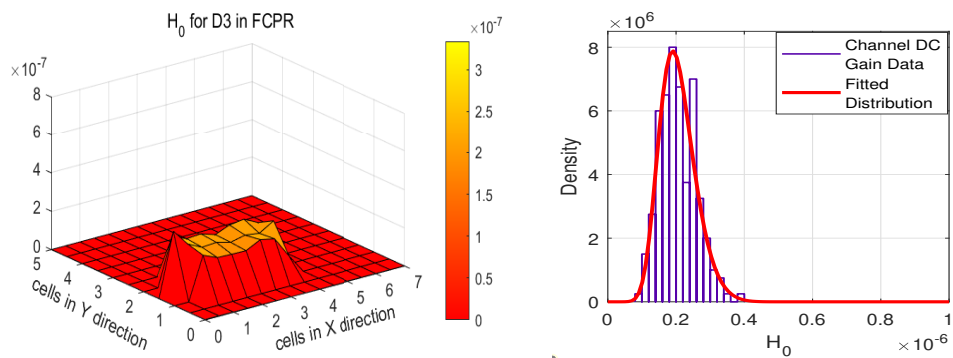
Figure 4.13: Spatial distribution and histogram of channel DC gains associated with D3. Left: Spatial distribution of H_0 for D3. Right: Generalized extreme value approximation to H_0 histogram of D3.
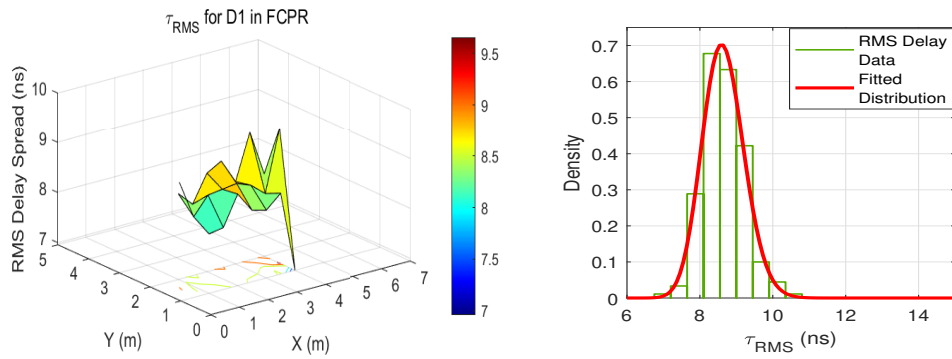
Figure 4.14: Spatial distribution and histogram of RMS delay spreads associated with D1. Left: Spatial distribution of τ_{RMS} for D1. Right: Log-normal distribution approximation to τ_{RMS} histogram of D1.
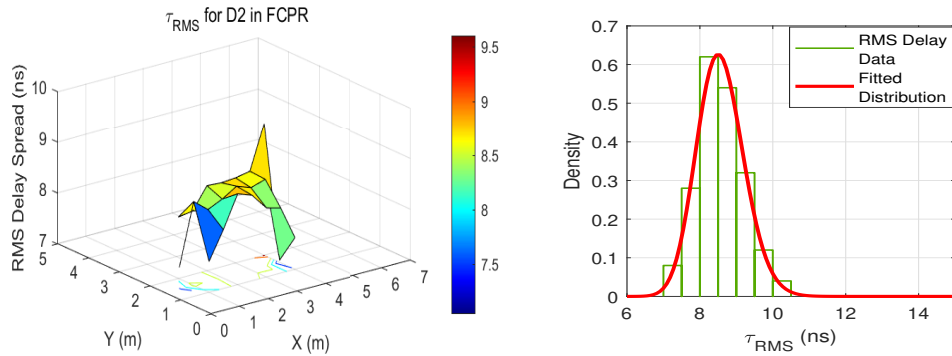
Figure 4.15: Spatial distribution and histogram of RMS delay spreads associated with D2. Left: Spatial distribution of τ_{RMS} for D1. Right: Log-normal distribution approximation to τ_{RMS} histogram of D2.
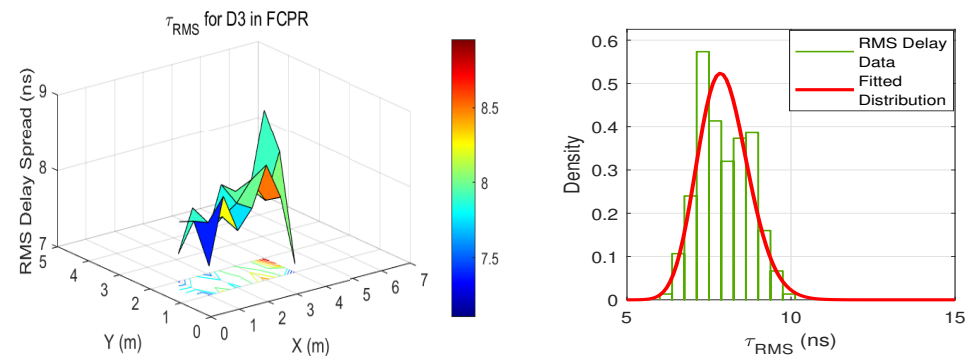
Figure 4.16: Spatial distribution and histogram of RMS delay spreads associated with D3. Left: Spatial distribution of τ_{RMS} for D3. Right: Log-normal distribution approximation to τ_{RMS} histogram of D3.

Chapter 5

Future Works

Although we addressed the major issues that researchers have been encountered, there are still many challenges we must work on to obviate. These open issues are summarized briefly as below.

If a patient wearing an MBSN node on the front side, falls on the ground then corresponding MBSN node may not communicate with the other end that should be calling for help, due to the complete blockage. Therefore, diversity techniques could be potentially applied to tackle this vital issue.

Wireless technology requires low power consumption which is especially true for subdermal MBNS nodes. Replacement or charging of the implanted MBSN node is extremely difficult. Thus, energy harvesting, which is the utilization of the ambient energy can be a solution to this critical issue.

Patient body movement induces the mobility of sensor-coupled transceiver in terms of location and orientation. Although obtaining a CIR for each sample point through randomly generated trajectory mitigated the problem of uncertainty, it is still a significant challenge for channel modeling and characterization of MBSNs.

Moreover, the mobility of the MBSNs nodes in an environment causes fluctuations in the received power. An appropriate model for link adaptation which combines LEDs in a most efficient way and selects modulation order, can be proposed to overcome this challenge.

Furthermore, the non-linearity of an LED source, multipath time dispersion, and the mobility of MBSNs node establish a time-varying VLC channel model. To obviate these channel capacity-limiting problems, a pre-distortion technique or a more realistic post-distortion technique can be proposed in the future works of the researchers. This indeed calls for the joint application of Reproducing Kernel Hilbert Space (RKHS) based methods with Information Theoretic Learning (ITL). Regarding these methods, recent works for different applications as VLC, massive MIMO, multiple-access localization [94–99] provide rigorous analytical results for the scenario-invariant and system-independent optimality of these approaches in presence of unknown nonlinearities and impairments.

Chapter 6

Conclusions

In this thesis, we presented a comprehensive overview of the VLC-based medical body sensor networks channel modeling which enables researchers to design their systems in best possible QoS. First we analyzed existing IR-based MBSNs channel models from which VLC channel models are derived. Thereafter, we scrutinized existing VLC-based MBSNs channel models according to the mobility of the MBSNs on the patient's body. The main criticisms among many other simplistic assumptions were the omission of the wavelength-dependency in modeling of the surface reflectance in VLC systems and lack of a proper skin channel model.

Moreover, we presented a novel approach for VLC-based channel modeling and characterization of the skin tissue. It was observed from these channel models that the detected rays which had experienced less number of events and hence the delays, manifested themselves as a steeper line in CIR. On the other hand, a gradual decrease in received power occurred due to the collection of power losing scattered rays.

Furthermore, we designed four different real-life based hospital scenarios to model and characterize the downlink VLC-based MBSN channels. For this reason, we utilized a site-specific non-sequential MCRT method to obtain CIRs in: i) ICU ward; ii) clinic; iii) semi-private hospital room; and iv) family-centered hospital

room. We then presented four sample CIRs for each scenario and their corresponding inferences. The effect of LED emitters were also taken into account to obtain the effective channel frequency response.

On the other hand, we considered the impact of 3D user mobility for two of the aforementioned hospital scenarios and hence we proposed an algorithm that generates a random trajectory by considering random step length and direction. Through the instrument of this algorithm and hence the extracted random trajectories, we carried out an extensive simulation study to model the mobile VLC-based MBSNs channels.

Based on simulation results, we reason that the channel DC gain values for D3, which is placed around the ankle, behave stably due to the collection of only NLoS rays. However, a sinusoidal manner in channel DC gain is exhibited for D1 and D2 when the body approaches and moves away from the luminaries. Furthermore, the maximum values of RMS delay spread in ICU ward and family type patient room are 14.22 ns and 10.61 ns, respectively. Consequently, we can model flat fading MBSNs channels for the former and the latter scenarios if the data rates are lower than 7.03 Mbit/s, and 9.43 Mbit/s, respectively.

After we show the spatial distribution of channel DC gains and RMS delays for the ICU ward and family-centered patient room scenarios, we present the statistical distribution of these channel characteristics as PDFs. We found out that generalized extreme value distribution fitted well for channel DC gain. The most probable channel DC gain values associated with D1 and D2 were similar and they were larger than that of D3, which was placed on the ankle, for both scenarios. On the other hand, log-normal distribution fitted well for RMS delay spreads. The most probable RMS delay spread values associated with D1–D3 were quite similar within each scenario. The distribution parameter values were consistent with histograms and the parameter value discrepancies between these two scenarios were due to the differences in room volumes of these scenarios.

References

[1] S. Arnon, J. Barry, G. Karagiannidis, R. Schober, and M. Uysal, *Advanced optical wireless communication systems*, 1st ed. Cambridge University Press, 2012.

[2] Z. Ghassemlooy, W. Popoola, and S. Rajbhandari, *Optical wireless communications: System and channel modelling with MATLAB*, 1st ed. CRC Press, 2017.

[3] D. Karunatilaka, F. Zafar, V. Kalavally, and R. Parthiban, "LED based indoor visible light communications: State of the art," *IEEE Communications Surveys & Tutorials*, vol. 17, no. 3, pp. 1649–1678, 2015.

[4] S. Arnon, *Visible light communication*, 1st ed. Cambridge University Press, 2015.

[5] S. Dimitrov and H. Haas, *Principles of LED light communications: Towards networked Li-Fi*, 1st ed. Cambridge University Press, 2015.

[6] Z. Ghassemlooy, L. N. Alves, S. Zvanovec, and M. A. Khalighi, *Visible light communications: Theory and applications*, 1st ed. CRC Press, 2017.

[7] A. Julien-Vergonjanne, S. Sahuguède, and L. Chevalier, "Optical wireless body area networks for healthcare applications," in *Optical wireless communications: An emerging technology*, M. Uysal, C. Capsoni, Z. Ghassemlooy, A. Boucouvalas, and E. Udvary, Eds. Springer International Publishing, 2016, pp. 569–587.

[8] "Medical electrical equipment-Part 1-2: General requirements for basic safety and essential performance-Collateral standard: Electromagnetic disturbances-Requirements and tests," 2014, IEC 60601-2.

[9] T. Cogalan and H. Haas, "Why would 5G need optical wireless communications?" in *2017 IEEE 28th Annual International Symposium on Personal, Indoor, and Mobile Radio Communications (PIMRC)*, 2017, pp. 1–6.

[10] P. H. Pathak, X. Feng, P. Hu, and P. Mohapatra, "Visible light communication, networking, and sensing: A survey, potential and challenges," *IEEE Communications Surveys & Tutorials*, vol. 17, no. 4, pp. 2047–2077, 2015.

[11] J. Luo, L. Fan, and H. Li, "Indoor positioning systems based on visible light communication: State of the art," *IEEE Communications Surveys & Tutorials*, vol. 19, no. 4, pp. 2871–2893, 2017.

[12] Y. Qiu, H.-H. Chen, and W.-X. Meng, "Channel modeling for visible light communications—A survey," *Wireless Communications and Mobile Computing*, vol. 16, no. 14, pp. 2016–2034, 2016.

[13] A. Al-Kinani, C. Wang, L. Zhou, and W. Zhang, "Optical wireless communication channel measurements and models," *IEEE Communications Surveys & Tutorials*, vol. 20, no. 3, pp. 1939–1962, 2018.

[14] D. C. O'Brien, L. Zeng, H. Le-Minh, G. Faulkner, J. W. Walewski, and S. Randel, "Visible light communications: Challenges and possibilities," in *2008 IEEE 19th International Symposium on Personal, Indoor and Mobile Radio Communications*, 2008, pp. 1–5.

[15] D. C. O'Brien, "Visible light communications: Challenges and potential," in *IEEE Photonic Society 24th Annual Meeting*, 2011, pp. 365–366.

[16] A. Jovicic, J. Li, and T. Richardson, "Visible light communication: Opportunities, challenges and the path to market," *IEEE Communications Magazine*, vol. 51, no. 12, pp. 26–32, 2013.

[17] "ISO/IEEE international standard health informatics-Point-of-care medical device communication-Transport profile-Infrared," 2004, ISO/IEEE 11073-30300:2004(E).

[18] "Safety of laser products—Part 1: Equipment classification and requirement," 2007, IEC60825-1.

[19] "Photo-biological safety of lamps and lamp systems (Identical with CIE S009)," 2006, IEC62471.

[20] A. Hadjidj, M. Souil, A. Bouabdallah, Y. Challal, and H. Owen, "Wireless sensor networks for rehabilitation applications: Challenges and opportunities," *Journal of Network and Computer Applications*, vol. 36, no. 1, pp. 1–15, 2013.

[21] F. R. Gfeller and U. Bapst, "Wireless in-house data communication via diffuse infrared radiation," *Proceedings of the IEEE*, vol. 67, no. 11, pp. 1474–1486, 1979.

[22] J. R. Barry, J. M. Kahn, W. J. Krause, E. A. Lee, and D. G. Messerschmitt, "Simulation of multipath impulse response for indoor wireless optical channels," *IEEE Journal on Selected Areas in Communications*, vol. 11, no. 3, pp. 367–379, 1993.

[23] F. J. López-Hernández and M. Betancor, "Dustin: Algorithm for calculation of impulse response on IR wireless indoor channels," *Electronics Letters*, vol. 33, pp. 1804–1806, 1997.

[24] M. Abtahi and H. Hashemi, "Simulation of indoor propagation channel at infrared frequencies in furnished office environments," in *Proceedings of 6th International Symposium on Personal, Indoor and Mobile Radio Communications*, 1995, pp. 306–310.

[25] J. B. Carruthers and P. Kannan, "Iterative site-based modeling for wireless infrared channels," *IEEE Transactions on Antennas and Propagation*, vol. 50, no. 5, pp. 759–765, 2002.

[26] J. B. Carruthers and J. M. Kahn, "Modeling of nondirected wireless infrared channels," *IEEE Transactions on Communications*, vol. 45, no. 10, pp. 1260–1268, 1997.

[27] V. Jungnickel, V. Pohl, S. Nonnig, and C. von Helmolt, "A physical model of the wireless infrared communication channel," *IEEE Journal on Selected Areas in Communications*, vol. 20, no. 3, pp. 631–640, 2002.

[28] N. Hayasaka and T. Ito, "Channel modeling of nondirected wireless infrared indoor diffuse link," *Electronics and Communications in Japan (Part I: Communications)*, vol. 90, no. 6, pp. 9–19, 2007.

[29] F. J. López-Hernández, R. Pérez-Jiménez, and A. Santamaria, "Monte Carlo calculation of impulse response on diffuse IR wireless indoor channels," *Electronics Letters*, vol. 34, pp. 1260–1262, 1998.

[30] F. Hernández, R. Pérez-JIménez, and A. Santamaría, "Modified Monte Carlo scheme for high-efficiency simulation of the impulse response on diffuse IR wireless indoor channels," *Electronics Letters*, vol. 34, pp. 1819–1820, 1998.

[31] M. I. S. Chowdhury, W. Zhang, and M. Kavehrad, "Combined deterministic and modified Monte Carlo method for calculating impulse responses of indoor optical wireless channels," *Journal of Lightwave Technology*, vol. 32, no. 18, pp. 3132–3148, 2014.

[32] S. Dimitrov, R. Mesleh, H. Haas, M. Cappitelli, M. Olbert, and E. Bassow, "On the SIR of a cellular infrared optical wireless system for an aircraft," *IEEE Journal on Selected Areas in Communications*, vol. 27, no. 9, pp. 1623–1638, 2009.

[33] H. Q. Nguyen, J. H. Choi, M. Kang, Z. Ghassemlooy, D. H. Kim, S. K. Lim, T. G. Kang, and C. G. Lee, "A MATLAB-based simulation program for indoor visible light communication system," in *2010 7th International Symposium on Communication Systems, Networks Digital Signal Processing (CSNDSP 2010)*, 2010, pp. 537–541.

[34] S. Long, M. Khalighi, M. Wolf, S. Bourennane, and Z. Ghassemlooy, "Channel characterization for indoor visible light communications," in *2014 3rd International Workshop in Optical Wireless Communications (IWOW)*, 2014, pp. 75–79.

[35] K. Lee, H. Park, and J. R. Barry, "Indoor channel characteristics for visible light communications," *IEEE Communications Letters*, vol. 15, no. 2, pp. 217–219, 2011.

[36] J. Ding, I. Chin-Lin, and Z. Xu, "Indoor optical wireless channel characteristics with distinct source radiation patterns," *IEEE Photonics Journal*, vol. 8, no. 1, pp. 1–15, 2016.

[37] H. Schulze, "Frequency-domain simulation of the indoor wireless optical communication channel," *IEEE Transactions on Communications*, vol. 64, no. 6, pp. 2551–2562, 2016.

[38] C. Chen, D. Basnayaka, and H. Haas, "Non-line-of-sight channel impulse response characterisation in visible light communications," in *2016 IEEE International Conference on Communications (ICC)*, 2016, pp. 1–6.

[39] A. Al-Kinani, C. Wang, H. Haas, and Y. Yang, "Characterization and modeling of visible light communication channels," in *2016 IEEE 83rd Vehicular Technology Conference (VTC Spring)*, 2016, pp. 1–5.

[40] ——, "A geometry-based multiple bounce model for visible light communication channels," in *2016 International Wireless Communications and Mobile Computing Conference (IWCMC)*, 2016, pp. 31–37.

[41] J. H. Lee and H. S. Lee, "A photon modeling method for characterization of indoor optical wireless system," *The Journal of Korean Institute of Electromagnetic Engineering and Science*, vol. 19, no. 6, pp. 688–697, 2008.

[42] S. P. Rodríguez, R. P. Jiménez, B. R. Mendoza, F. J. L. Hernández, and A. J. A. Alfonso, "Simulation of impulse response for indoor visible light

communications using 3D CAD models," *EURASIP Journal on Wireless Communications and Networking*, vol. 2013, no. 1, pp. 1–10, 2013.

[43] F. Miramirkhani and M. Uysal, "Channel modeling and characterization for visible light communications," *IEEE Photonics Journal*, vol. 7, no. 6, pp. 1–16, 2015.

[44] J. Rufo, J. Rabadan, V. Guerra, and R. Perez-Jimenez, "BRDF models for the impulse response estimation in indoor optical wireless channels," *IEEE Photonics Technology Letters*, vol. 29, no. 17, pp. 1431–1434, 2017.

[45] M. Uysal, F. Miramirkhani, O. Narmanlioglu, T. Baykas, and E. Panayirci, "IEEE 802.15.7r1 reference channel models for visible light communications," *IEEE Communications Magazine*, vol. 55, no. 1, pp. 212–217, 2017.

[46] F. Miramirkhani, O. Narmanlioglu, M. Uysal, and E. Panayirci, "A mobile channel model for VLC and application to adaptive system design," *IEEE Communications Letters*, vol. 21, no. 5, pp. 1035–1038, 2017.

[47] F. Miramirkhani and M. Uysal, "Channel modelling for indoor visible light communications," *Philosophical Transactions of the Royal Society A, Special Issue on The Cross-Disciplinary Challenges towards Mobile Optical Wireless Networks*, vol. 378, no. 2169, pp. 20 190 187–20 190 187, 2020.

[48] S. S. Torkestani, A. Julien-Vergonjanne, and J. P. Cances, "Mobile health-care monitoring in hospital based on diffuse optical wireless technology," in *21st Annual IEEE International Symposium on Personal, Indoor and Mobile Radio Communications*, 2010, pp. 1055–1059.

[49] S. S. Torkestani, N. Barbot, S. Sahuguede, A. Julien-Vergonjanne, and J. P. Cances, "Performance and transmission power bound analysis for optical wireless based mobile healthcare applications," in *2011 IEEE 22nd International Symposium on Personal, Indoor and Mobile Radio Communications*, 2011, pp. 2198–2202.

[50] S. S. Torkestani, A. Julien-Vergonjanne, and J. P. Cances, "Indoor optical wireless system dedicated to healthcare application in hospital," in *2010 7th International Symposium on Communication Systems, Networks Digital Signal Processing (CSNDSP 2010)*, 2010, pp. 542–546.

[51] S. S. Torkestani, S. Sahuguede, A. Julien-Vergonjanne, J. Cances, and J. C. Daviet, "Infrared communication technology applied to indoor mobile healthcare monitoring system," *International Journal of E-Health and Medical Communications*, vol. 3, no. 3, pp. 1–11, 2012.

[52] E. A. Alyan and S. A. Aljunid, "Development of wireless optical CDMA system for biosignal monitoring," *Optik*, vol. 145, pp. 250–257, 2017.

[53] A. M. Khalid, G. Cossu, and E. Ciaramella, "Diffuse IR-optical wireless system demonstration for mobile patient monitoring in hospitals," in *2013 15th International Conference on Transparent Optical Networks (ICTON)*, 2013, pp. 1–4.

[54] P. Toumieux, L. Chevalier, S. Sahuguède, and A. Julien-Vergonjanne, "Optical wireless connected objects for healthcare," *Healthcare Technology Letters*, vol. 2, no. 5, pp. 118–122, 2015.

[55] C. L. Bas, L. Chevalier, P. Toumieux, S. Sahuguede, and A. Julien-Vergonjanne, "Experimental study of an optical wireless physical activity monitoring system," in *2016 10th International Symposium on Medical Information and Communication Technology (ISMICT)*, 2016, pp. 1–5.

[56] T. B. Hoang, S. Sahuguede, and A. Julien-Vergonjanne, "Behavior of non-directed optical wireless channel considering receiver orientation," in *2017 20th International Symposium on Wireless Personal Multimedia Communications (WPMC)*, 2017, pp. 223–228.

[57] T. B. Hoang, S. Kandukuri, S. Sahuguede, and A. Julien-Vergonjanne, "Infrared mobile transmissions for smart indoor applications," in *2018 11th International Symposium on Communication Systems, Networks Digital Signal Processing (CSNDSP)*, 2018, pp. 1–6.

[58] A. Kaba, S. Sahuguede, and A. Julien-Vergonjanne, "Channel modeling of an optical wireless body sensor network for walk monitoring of elderly," *Sensors*, vol. 21, no. 9, pp. 1–19, 2021.

[59] Y. Cheong, X. Ng, and W. Chung, "Hazardless biomedical sensing data transmission using VLC," *IEEE Sensors Journal*, vol. 13, no. 9, pp. 3347–3348, 2013.

[60] C. L. Bas, S. Sahuguede, A. Julien-Vergonjanne, A. Behlouli, P. Combeau, and L. Aveneau, "Impact of receiver orientation and position on visible light communication link performance," in *2015 4th International Workshop on Optical Wireless Communications (IWOW)*, 2015, pp. 1–5.

[61] ——, "Human body impact on mobile visible light communication link," in *2016 10th International Symposium on Communication Systems, Networks and Digital Signal Processing (CSNDSP)*, 2016, pp. 1–6.

[62] A. Behlouli, P. Combeau, S. Sahuguède, A. Julien-Vergonjanne, C. L. Bas, and L. Aveneau, "Impact of physical and geometrical parameters on visible light communication links," in *2017 Advances in Wireless and Optical Communications (RTUWO)*, 2017, pp. 73–76.

[63] C. L. Bas, T. B. Hoang, S. Sahuguede, and A. Julien-Vergonjanne, "Lighting fixture communicating in infrared and visible for indoor health monitoring," in *2017 IEEE 19th International Conference on E-Health Networking, Applications and Services (Healthcom)*, 2017, pp. 1–6.

[64] C. Lebas, S. Sahuguede, A. Julien-Vergonjanne, P. Combeau, and L. Aveneau, "Infrared and visible links for medical body sensor networks," in *2018 Global LIFI Congress (GLC)*, 2018, pp. 1–6.

[65] T. Hoang, S. Sahuguede, and A. Julien-Vergonjanne, "Optical wireless network design for off-body-sensor based monitoring," *Wireless Communications and Mobile Computing*, vol. 2019, pp. 1–13, 2019.

[66] A. A. Farid and S. Hranilovic, "Outage capacity optimization for free-space optical links with pointing errors," *Journal of Lightwave Technology*, vol. 25, no. 7, pp. 1702–1710, 2007.

[67] L. Chevalier, S. Sahuguede, A. Julien-Vergonjanne, P. Combeau, and L. Aveneau, "Investigation of wireless optical technology for communication between on-body nodes," in *2013 2nd International Workshop on Optical Wireless Communications (IWOW)*, 2013, pp. 79–83.

[68] L. Chevalier, S. Sahuguede, and A. Julien-Vergonjanne, "Investigation of obstacle effect on wireless optical on-body communication performance," in *2014 21st International Conference on Telecommunications (ICT)*, 2014, pp. 103–107.

[69] ——, "Performance evaluation of wireless optical communication for mobile BAN scenario with blocking effects," in *2014 9th International Symposium on Communication Systems, Networks Digital Sign (CSNDSP)*, 2014, pp. 319–324.

[70] ——, "Wireless optical technology based body area network for health monitoring application," in *2015 IEEE International Conference on Communications (ICC)*, 2015, pp. 2863–2868.

[71] O. Haddad, M. A. Khalighi, S. Zvanovec, and M. Adel, "Channel characterization and modeling for optical wireless body-area networks," *IEEE Open Journal of the Communications Society*, vol. 1, pp. 760–776, 2020.

[72] W. Noonpakdee, "Performance analysis of passive - active optical wireless transmission for personal health monitoring," in *2014 Sixth International Conference on Ubiquitous and Future Networks (ICUFN)*, 2014, pp. 17–21.

[73] Y.-Y. Tan and W.-Y. Chung, "Mobile health-monitoring system through visible light communication," *Bio-Medical Materials and Engineering*, vol. 24, no. 6, pp. 3529–3538, 2014.

[74] W. A. Cahyadi, T. Jeong, Y. Kim, Y. Chung, and T. Adiono, "Patient monitoring using visible light uplink data transmission," in *2015 International Symposium on Intelligent Signal Processing and Communication Systems (ISPACS)*, 2015, pp. 431–434.

[75] V. P. Rachim, J. An, P. N. Quan, and W. Chung, "A novel smartphone camera-LED communication for clinical signal transmission in mhealth-rehabilitation system," in *2017 39th Annual International Conference of the IEEE Engineering in Medicine and Biology Society (EMBC)*, 2017, pp. 3437–3440.

[76] M. Uysal, F. Miramirkhani, T. Baykas, and K. Qaraqe, "IEEE 802.11bb Reference Channel Models for Indoor Environments," 2018, doc.: IEEE 11-18-1582-02-00bb.

[77] T. Maeda, N. Arakawa, M. Takahashi, and Y. Aizu, "Monte Carlo simulation of spectral reflectance using a multilayered skin tissue model," *Optical Review (Tokyo, Japan)*, vol. 17, no. 3, pp. 223–229, 2010.

[78] I. V. Meglinski and S. J. Matcher, "Quantitative assessment of skin layers absorption and skin reflectance spectra simulation in the visible and near-infrared spectral regions," *Physiological Measurement*, vol. 23, no. 4, pp. 741–753, 2002.

[79] R. Liang, *Optical design for biomedical imaging*, 1st ed. SPIE, 2010.

[80] C. R. Simpson, M. Kohl, M. Essenpreis, and M. Cope, "Near-infrared optical properties of ex vivo human skin and subcutaneous tissues measured using the Monte Carlo inversion technique," *Physics in Medicine & Biology*, vol. 43, no. 9, pp. 2465–2478, 1998.

[81] D. M. Ackermann, B. Smith, X. F. Wang, K. L. Kilgore, and P. H. Peckham, "Designing the optical interface of a transcutaneous optical telemetry link," *IEEE Transactions on Biomedical Engineering*, vol. 55, no. 4, pp. 1365–1373, 2008.

[82] W. A. G. Bruls and J. C. Van Der Leun, "Forward scattering properties of human epidermal layers," *Photochemistry and Photobiology*, vol. 40, no. 2, pp. 231–242, 1984.

[83] T. Lister, P. A. Wright, and P. H. Chappell, "Optical properties of human skin," *Journal of Biomedical Optics*, vol. 17, no. 9, pp. 90 901–90 901, 2012.

[84] G. Appelboom, E. Camacho, M. E. Abraham, S. S. Bruce, E. L. P. Dumont, B. E. Zacharia, R. D'Amico, J. Slomian, J. Y. Reginster, O. Bruyère, and E. S. Connolly, "Smart wearable body sensors for patient self-assessment and monitoring," *Archives of Public Health*, vol. 72, no. 1, pp. 28–28, 2014.

[85] V. Dremin, E. Zherebtsov, A. Bykov, A. Popov, A. Doronin, and I. Meglinski, "Influence of blood pulsation on diagnostic volume in pulse oximetry and photoplethysmography measurements," *Applied Optics*, vol. 58, no. 34, pp. 9398–9405, 2019.

[86] F. P. Bolin, L. E. Preuss, R. C. Taylor, and R. J. Ference, "Refractive index of some mammalian tissues using a fiber optic cladding method," *Applied Optics*, vol. 28, no. 12, pp. 2297–2303, 1989.

[87] F. Miramirkhani and M. Uysal, "Visible light communication channel modeling for underwater environments with blocking and shadowing," *IEEE Access*, vol. 6, pp. 1082–1090, 2018.

[88] Facility guidelines institute (FGI), "Interim amendment for the 2018 residential guidelines," 2020, Guidelines for design and construction of residential health, care, and support facilities. [Online]. Available: https://fgiguidelines.org/wp-content/uploads/2020/08/FGI-2018-RES-Interim-Amendment-ResidentRooms_2020-08-28.pdf

[89] State of Kuwait ministry of health infection control directorate, "Guidelines for general ward design," 2008. [Online]. Available: http://www.icdkwt.com/pdf/policiesandguidelines/DesignandConstruction/GuidelinesforGeneralWardDesign-2008.pdf

[90] Illuminating engineering society (IES) of North America, "Lighting for hospitals and healthcare facilities," 2016, aNSI/IES RP-29-16.

[91] T. Komine, J. H. Lee, S. Haruyama, and M. Nakagawa, "Adaptive equalization system for visible light wireless communication utilizing multiple white LED lighting equipment," *IEEE Transactions on Wireless Communications*, vol. 8, no. 6, pp. 2892–2900, 2009.

[92] S. Kotz and S. Nadarajah, *Extreme Value Distributions*. Imperial College Press, 2000.

[93] N. L. Johnson, S. Kotz, and N. Balakrishnan, *Continuous Univariate Distributions*, 2nd ed., ser. Wiley Series in Probability and Statistics. Wiley-Interscience, New York, NY (USA), 1994.

[94] R. Mitra, G. Kaddoum, and V. Bhatia, "Hyperparameter-free transmit-nonlinearity mitigation using a kernel-width sampling technique," *IEEE Transactions on Communications*, vol. 69, no. 4, pp. 2613–2627, 2020.

[95] E. Sfeir, R. Mitra, G. Kaddoum, and V. Bhatia, "RFF based detection for SCMA in presence of PA nonlinearity," *IEEE Communications Letters*, vol. 24, no. 11, pp. 2604–2608, 2020.

[96] ——, "Performance analysis of maximum-correntropy based detection for SCMA," *IEEE Communications Letters*, vol. 25, no. 4, pp. 1114–1118, 2020.

[97] R. Mitra, F. Miramirkhani, V. Bhatia, and M. Uysal, "Low complexity least minimum symbol error rate based post-distortion for vehicular VLC," *IEEE Transactions on Vehicular Technology*, vol. 69, no. 10, pp. 11 800–11 810, 2020.

[98] R. Mitra, S. Jain, and V. Bhatia, "Least minimum symbol error rate based post-distortion for VLC using random Fourier features," *IEEE Communications Letters*, vol. 24, no. 4, pp. 830–834, 2020.

[99] R. Mitra, G. Kaddoum, G. Dahman, and G. Poitau, "Error analysis of localization based on minimum-error entropy with fiducial points," *IEEE Communications Letters*, vol. 25, no. 4, pp. 1187–1191, 2020.